Journal of *Marine Science and Engineering*

MDPI

Article

Elliptical Disk-Based Collision Avoidance for Formation Tracking Control of Underactuated Surface Vessels Under Input Saturation

Yafei Ge and Xiaoming Xia *

School of Ocean Engineering, Jiangsu Ocean University, Lianyungang 222005, China; ge_yafei@163.com
* Correspondence: xia_xm@126.com

Abstract

This paper investigates a formation tracking problem for underactuated surface vessels (USVs) subject to collision avoidance and input saturation constraints. Many existing APF-based formation-control approaches formulate collision avoidance using a single reference point or an inter-center distance, which may provide insufficient geometric information during close-range maneuvers. To improve navigation safety, an elliptical disk-based collision avoidance mechanism is developed by introducing safety points at the bow, stern, port, and starboard sides of each USV, such that multiple characteristic-point distance constraints can be simultaneously enforced. To address unknown nonlinearities caused by model uncertainties and external disturbances, a neural network-based observer is designed to estimate unavailable velocity states and lumped disturbances. Distributed control laws are synthesized by integrating artificial potential functions (APFs), the observer, and a backstepping technique. Additional controllers are introduced to address the input saturation and underactuated issues while preserving the collision avoidance capability. Stability of the closed-loop system is rigorously established via Lyapunov theory. Simulation results demonstrate that the proposed approach achieves safer close-range maneuvering performance compared with conventional single-point methods.

Keywords: underactuated surface vessels; formation tracking; elliptical disk-based collision avoidance; input saturation; artificial potential function

1. Introduction

Over the past two decades, unmanned surface vehicles (USVs) have been increasingly employed in environmental monitoring, hydrographic and oceanographic surveying, maritime surveillance, and search-and-rescue support owing to their autonomy, operational flexibility, and ability to perform missions in hazardous marine environments [1]. Formation control aims to coordinate multiple USVs to follow prescribed trajectories while maintaining desired geometric configurations. Representative formation-control architectures include behavior-based and virtual-structure methods [2,3], leader–follower strategies [4,5], and graph-based distributed schemes [6–9]. Among them, distributed graph-based approaches are particularly attractive because formation objectives can be achieved using only local interaction information.

Collision avoidance is essential for safe USV operations, especially in confined waterways, congested ports, and dynamic maritime environments where close-range maneuvers are frequently required. Existing collision-avoidance schemes for USV

Check for updates

Academic Editor: Weicheng Cui

Received: 29 July 2026
Revised: 18 August 2026
Accepted: 19 August 2026
Published: 21 August 2026

Copyright: © 2026 by the authors. Licensee MDPI, Basel, Switzerland. This article is an open access article distributed under the terms and conditions of the Creative Commons Attribution (CC BY) license.

formations and related multi-agent systems mainly include formation-reconfiguration methods [10,11], prescribed-performance, error-transformation, or barrier-function-based methods [8,9,12,13], and artificial-potential-function-based methods [3,14–17]. Formation-reconfiguration methods avoid collisions by temporarily modifying the desired geometric configuration or interaction topology [10,11], but their implementation requires an appropriate switching or reconfiguration strategy. Prescribed-performance and error-transformation methods enforce safety constraints through transformed tracking errors or barrier-type functions; however, the required control action may increase significantly as the system states approach the prescribed boundaries [18], which complicates their application to systems subject to actuator saturation. In contrast, artificial potential function (APF)-based methods provide a convenient means of incorporating repulsive interactions into distributed formation controllers.

A common simplification in representative APF-based USV studies is to construct collision-avoidance terms using vessel reference positions or inter-center distances [3,16]. Although this formulation facilitates controller design, a single reference distance does not explicitly distinguish the clearances associated with the bow, stern, port, and starboard regions during close-range encounters. Existing studies have accounted for vehicle dimensions by approximating mobile agents or underactuated ships using elliptical shapes [19,20]. Ship-domain approaches have also introduced direction-dependent fore, aft, port, and starboard dimensions to describe nonuniform navigational safety margins [21,22]. These studies demonstrate the importance of incorporating vessel geometry and encounter orientation into collision-risk assessment. Recent studies have continued to advance formation and collision-avoidance control for multi-USV systems. Yoo and Park investigated distributed formation control with dynamic obstacle avoidance for uncertain underactuated surface vehicles under a directed network [23]. Liu et al. developed an adaptive output feedback event-triggered formation-control scheme with an obstacle-avoidance mechanism for underactuated ships [24]. In addition, a recent bibliometric study provides an updated overview of the development and research trends of multi-USV formation control [25]. Nevertheless, the existing studies, including these recent developments, do not jointly incorporate multiple body-fixed characteristic-point constraints into observer-based formation control of uncertain underactuated USVs subject to unmeasured velocities and actuator saturation [6,8,9,15,17,26,27].

Motivated by this issue and building on established observer-based output feedback architectures for uncertain underactuated surface vessels [26,27], this paper develops a multi-point collision-avoidance measure based on an orientation-dependent virtual elliptical reference geometry. The ellipse is introduced to characterize the directional extent of a USV and to locate four representative safety points at the bow, stern, port, and starboard directions; it is not intended as an exact geometric reconstruction of the physical vessel hull. For two neighboring USVs, a point-based approximate proximity measure is defined as the minimum of the 16 pairwise distances generated by their respective characteristic safety points. This quantity is incorporated into the APFs to account for orientation-dependent local proximity information instead of relying only on a centroid-to-centroid distance. The resulting measure is used as a collision-risk indicator and is not interpreted as the exact Euclidean minimum distance between two elliptical boundaries or between two physical hulls.

Within the resulting control framework, an RBFNN-based observer is employed to recover the unmeasured surge, sway, and yaw velocities and approximate the lumped unknown dynamics arising from model uncertainties and environmental disturbances [26–28]. Distributed control laws are then constructed by combining the multi-point APFs, observer-based compensation, dynamic-surface filters, and backstepping design. Auxiliary

hyperbolic-tangent compensation dynamics are introduced to address underactuation and actuator saturation while preserving the collision-avoidance capability. Lyapunov analysis establishes the boundedness of all error signals in the resulting closed-loop system.

Figure 1 schematically illustrates the formation-tracking and collision-avoidance problem considered in this study, where four follower USVs are required to maintain prescribed formation relationships with respect to a virtual leader while avoiding inter-vessel collisions and static obstacles.

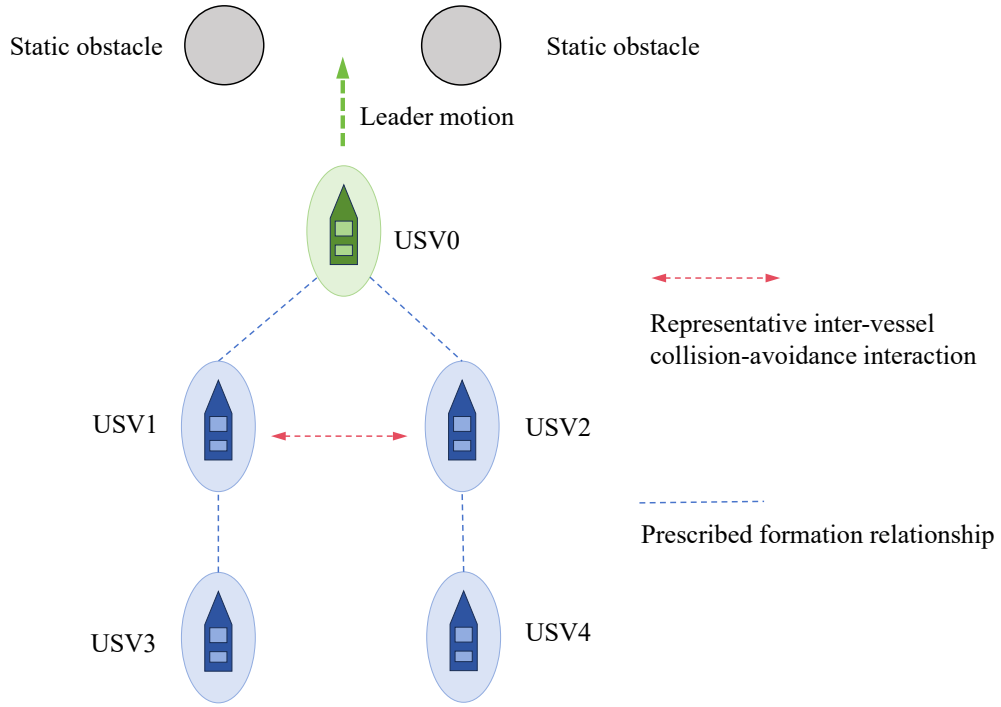


Figure 1. Schematic illustration of the formation-tracking and collision-avoidance problem considered in this study.

The main contributions of this paper are summarized as follows.

(1) A multi-point collision-avoidance measure based on an orientation-dependent virtual elliptical reference geometry is developed for close-range USV formation maneuvers. Four body-fixed characteristic safety points are assigned to each vessel, and the minimum of the resulting 16 point-pair distances is employed as a point-based approximate proximity measure in the APFs. Compared with a single-reference-point representation, the proposed measure incorporates additional orientation-dependent proximity information associated with the bow, stern, port, and starboard directions.

(2) The proposed multi-point safety measure is integrated into a distributed observer-based output feedback formation-control framework. The resulting controller simultaneously addresses formation tracking, static-obstacle avoidance, inter-vessel collision avoidance, unknown dynamics, unmeasured velocities, underactuation, and actuator saturation.

(3) Lyapunov analysis proves the boundedness of all closed-loop error signals. Comparative simulations conducted under identical initial conditions, disturbances, controller parameters, and actuator constraints show that the proposed method maintains the prescribed minimum safety-point distance in close-range encounters where a conventional centroid-based method may provide insufficient safety-point clearance.

2. Mathematical Preliminaries and Problem Formulation

2.1. Notation

The mathematical notation used in the subsequent analysis is specified as follows. The subscript $i \in \{1, \ldots, N\}$ is assigned to the individual USVs, with N being the total number of USVs. The symbols $|\cdot|$ and $\|\cdot\|$ are used for the absolute value and Euclidean norm, respectively. For a square matrix, $\lambda_{\min}(\cdot)$ and $\lambda_{\max}(\cdot)$ indicate its minimum and maximum eigenvalues. The operators $\max(\cdot)$ and $\min(\cdot)$ give the maximum and minimum values of a variable, respectively. A diagonal matrix is formed by $\mathrm{diag}\{\cdot\}$. The notation $\mathbb{R}^{m\times n}$ refers to the m-dimensional Euclidean space with n elements. Finally, I_n and 0_n stand for the $n \times n$ identity matrix and zero matrix, respectively.

2.2. Graph Theory

Graph theory is employed to describe the directed communication topology among the leader and follower USVs, following standard graph-based distributed formation-control formulations [2,7–9]. The framework is defined by a directed graph $\mathcal{G} = \{\mathcal{V}_\mathcal{G}, \Theta\}$. $\mathcal{V}_\mathcal{G} = \{0, 1, \ldots, N\}$ represents the set of all USVs. $\Theta = \{(i, j) \in \{1, \ldots, N\} \times \mathcal{V}_\mathcal{G}\}$ captures directional communication links. An edge $(i, j) \in \Theta$ indicates that the ith USV can access information from the jth USV. Two USVs are termed neighbors if their spatial proximity satisfies a predefined threshold. For the ith USV, its neighboring set at time t is denoted as $\mathcal{N}_i(t) = \{j \in \mathcal{V}_\mathcal{G}, (i, j) \in \Theta\}$.

The following directed spanning-tree condition is commonly adopted to ensure that the leader information can be transmitted to all follower USVs through the communication network [7–9].

Assumption 1. *At the initial time $t = 0$, the directed graph $\mathcal{G}$ contains a spanning tree oriented toward the leader, which serves as the root node.*

2.3. USV Model and Control Problem

A formation composed of N underactuated USVs is considered. Figure 2 illustrates the coordinate frames and motion variables associated with the ith USV. The sensing and communication hardware layers are not explicitly modeled in this study. The proposed control framework is formulated in terms of available position–heading measurements, control inputs, leader/neighbor information, and obstacle information. Therefore, the controller does not depend on a specific acoustic, ultrasonic, or electromagnetic sensing frequency. Following the standard three-degree-of-freedom (3-DOF) marine-craft kinematic and dynamic model presented in [29], the horizontal-plane motion of the ith USV is described by

$$\begin{aligned} \dot{\eta}_i &= J_i(\psi_i)\nu_i \\ \dot{\nu}_i &= \zeta_i + M_i^{-1}\tau_i, \end{aligned} \tag{1}$$

where x_i, y_i, and ψ_i specify the longitudinal position, lateral position, and yaw angle in the earth-fixed frame $X_E O_E Y_E$, respectively, and these variables form the position vector $\eta_i = [x_i, y_i, \psi_i]^{\mathrm{T}}$. In the body-fixed frame $X_B O_B Y_B$, the surge, sway, and yaw angular velocities are represented by u_i, v_i, and r_i, respectively, which are collected into the velocity vector $\nu_i = [u_i, v_i, r_i]^{\mathrm{T}}$. The mass distribution is characterized by the inertial matrix $M_i = \mathrm{diag}\{m_{i,11}, m_{i,22}, m_{i,33}\}$, whose diagonal elements $m_{i,11}$, $m_{i,22}$ and $m_{i,33}$ are associated with the surge, sway, and yaw inertial masses, respectively. The lumped uncertain term ζ_i represents the uncertain and unmodeled hydrodynamic dynamics together with time-

varying environmental disturbances. The control input vector $\tau_i = [\tau_{i,u}, 0, \tau_{i,r}]^{\mathrm{T}}$ includes the surge thrust $\tau_{i,u}$ and yaw moment $\tau_{i,r}$. The rotation matrix $J_i(\psi_i)$ is given as

$$J_i(\psi_i) = \begin{bmatrix} \cos(\psi_i) & -\sin(\psi_i) & 0 \\ \sin(\psi_i) & \cos(\psi_i) & 0 \\ 0 & 0 & 1 \end{bmatrix}.$$

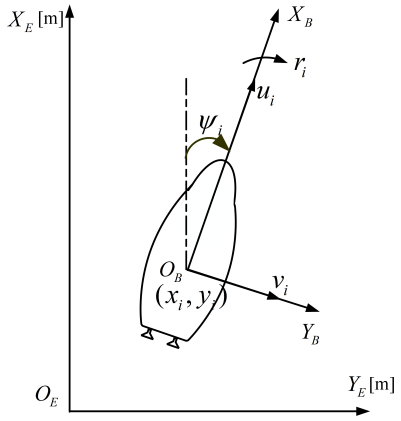


Figure 2. Reference frames and motion variables of the ith USV.

Assumption 2. *The derivative $\dot{v}_i$ is norm-bounded by an unknown positive constant v_i^*, i.e., $\|\dot{v}_i\| \leq v_i^*$.*

Assumption 3. *The time derivative of F_i is norm-bounded by an unknown positive constant F_i^*, i.e., $\|\dot{F}_i\| \leq F_i^*$.*

As illustrated in Figure 3, ρ_{ij} specifies the relative distance from the ith USV to leader j. The associated kinematic relations are expressed as:

$$\rho_{ij} = \sqrt{(x_j - x_i - p_{ijc})^2 + (y_j - y_i - p_{ijc})^2}, \tag{2}$$

$$\begin{aligned} \dot{\rho}_{ij} = & -u_i \cos(\psi_i - \lambda_{ij}) + u_j \cos(\psi_j - \lambda_{ij}) \\ & + v_i \sin(\psi_i - \lambda_{ij}) - v_j \sin(\psi_j - \lambda_{ij}) \\ & - \dot{p}_{ijc}[\cos(\lambda_{ij}) + \sin(\lambda_{ij})], \end{aligned} \tag{3}$$

where p_{ijc} is an artificial potential function used for collision avoidance, which will be defined later.

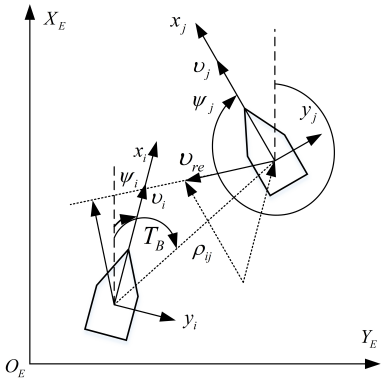


Figure 3. Leader–follower structure.

The relative angle λ_{ij} for the ith USV with respect to leader j is obtained from

$$\lambda_{ij} = \text{atan2}(y_j - y_i, x_j - x_i) \tag{4}$$

Differentiating λ_{ij} with respect to time yields

$$\begin{aligned}\dot{\lambda}_{ij} = \frac{1}{\rho_{ij}}\{&-u_i \sin(\psi_i - \lambda_{ij}) + u_j \sin(\psi_j - \lambda_{ij}) \\ &- v_i \cos(\psi_i - \lambda_{ij}) + v_j \cos(\psi_j - \lambda_{ij})\}.\end{aligned} \tag{5}$$

The desired formation behavior requires the ith USV to maintain the prescribed relative position with respect to leader j, expressed by

$$\begin{aligned}\lim_{t\to+\infty} |\rho_{ij} - \rho_{ij,d}| \le c_1, \\ \lim_{t\to+\infty} |\lambda_{ij} - \lambda_{ij,d}| \le c_2,\end{aligned} \tag{6}$$

where $\rho_{ij,d}$ and $\lambda_{ij,d}$ are desired distance and angle, c_1 and c_2 are tunable positive constants that can be set arbitrarily small.

In practical USV systems, both operational velocity limits and actuator constraints should be considered. Accordingly, the surge, sway, and yaw velocities are assumed to satisfy the following bounds, whereas the available surge force and yaw moment are subject to actuator saturation [9,26,30,31].

$$\begin{aligned}|u_i| \le \bar{u}_i, |v_i| \le \bar{v}_i, |r_i| \le \bar{r}_i \\ |u_j| \le \bar{u}_j, |v_j| \le \bar{v}_j, |r_j| \le \bar{r}_j\end{aligned} \tag{7}$$

where $\bar{u}_i$, $\bar{v}_i$, $\bar{r}_i$ are the bounds of u_i, v_i and r_i, respectively, while $\bar{u}_j$, $\bar{v}_j$, $\bar{r}_j$ are the bounds of u_j, v_j and r_j, respectively.

The command generated by the distributed controller is denoted by $\tau_{ic} = [\tau_{i,uc}, 0, \tau_{i,rc}]^{\mathrm{T}}$, where $\tau_{i,uc}$ and $\tau_{i,rc}$ correspond to the surge force and yaw moment, respectively. The actual control input after saturation is expressed as $\tau_i = [\tau_{i,u}, 0, \tau_{i,r}]^{\mathrm{T}}$. The effect of actuator saturation is quantified by the mismatch $\varpi_i = [\varpi_{i,u}, 0, \varpi_{i,r}]^{\mathrm{T}} = \tau_{ic} - \tau_i$. Accordingly, the relation between the commanded and saturated control inputs can be written as $\tau_i = \tau_{ic} - \varpi_i$.

Elliptical representations have been employed to account for the non-negligible dimensions and heading-dependent geometry of mobile agents and underactuated ships [19,20]. In the present work, the ellipse is introduced as a virtual orientation-dependent reference geometry rather than an exact representation of the physical USV hull. Four body-fixed characteristic safety points are placed at the endpoints of the major and minor axes of this virtual geometry, corresponding to the bow, stern, port, and starboard directions, respectively.

Lemma 1. *Let the elliptical disks i and j be represented by bounding ellipses centered at (x_i, y_i) and (x_j, y_j), respectively. Their heading angles are ψ_i and ψ_j, while the corresponding semi-axes are (a_i, b_i) and (a_j, b_j). The geometric configuration is illustrated in Figure 4. The generalized distance ρ_{ijc} associated with the two elliptical disks is defined as*

$$\rho_{ijc} = \min\left\{\begin{array}{l}\sqrt{(x_i - x_j + A_i - A_j)^2 + (y_i - y_j + B_i - B_j)^2},\\ \sqrt{(x_i - x_j + A_i + A_j)^2 + (y_i - y_j + B_i + B_j)^2},\\ \sqrt{(x_i - x_j + A_i - C_j)^2 + (y_i - y_j + B_i - D_j)^2},\\ \sqrt{(x_i - x_j + A_i + C_j)^2 + (y_i - y_j + B_i + D_j)^2},\\ \sqrt{(x_i - x_j - A_i - A_j)^2 + (y_i - y_j - B_i - B_j)^2},\\ \sqrt{(x_i - x_j - A_i + A_j)^2 + (y_i - y_j - B_i + B_j)^2},\\ \sqrt{(x_i - x_j - A_i - C_j)^2 + (y_i - y_j - B_i - D_j)^2},\\ \sqrt{(x_i - x_j - A_i + C_j)^2 + (y_i - y_j - B_i + D_j)^2},\\ \sqrt{(x_i - x_j + C_i - A_j)^2 + (y_i - y_j + D_i - B_j)^2},\\ \sqrt{(x_i - x_j + C_i + A_j)^2 + (y_i - y_j + D_i + B_j)^2},\\ \sqrt{(x_i - x_j + C_i - C_j)^2 + (y_i - y_j + D_i - D_j)^2},\\ \sqrt{(x_i - x_j + C_i + C_j)^2 + (y_i - y_j + D_i + D_j)^2},\\ \sqrt{(x_i - x_j - C_i - A_j)^2 + (y_i - y_j - D_i - B_j)^2},\\ \sqrt{(x_i - x_j - C_i + A_j)^2 + (y_i - y_j - D_i + B_j)^2},\\ \sqrt{(x_i - x_j - C_i - C_j)^2 + (y_i - y_j - D_i - D_j)^2},\\ \sqrt{(x_i - x_j - C_i + C_j)^2 + (y_i - y_j - D_i + D_j)^2}\end{array}\right\},$$

where $A_i = a_i\cos(\psi_i)$, $B_i = a_i\sin(\psi_i)$, $C_i = -b_i\sin(\psi_i)$, $D_i = -b_i\cos(\psi_i)$, $A_j = a_j\cos(\psi_j)$, $B_j = a_j\sin(\psi_j)$, $C_j = -b_j\sin(\psi_j)$ *and* $D_j = -b_j\cos(\psi_j)$.

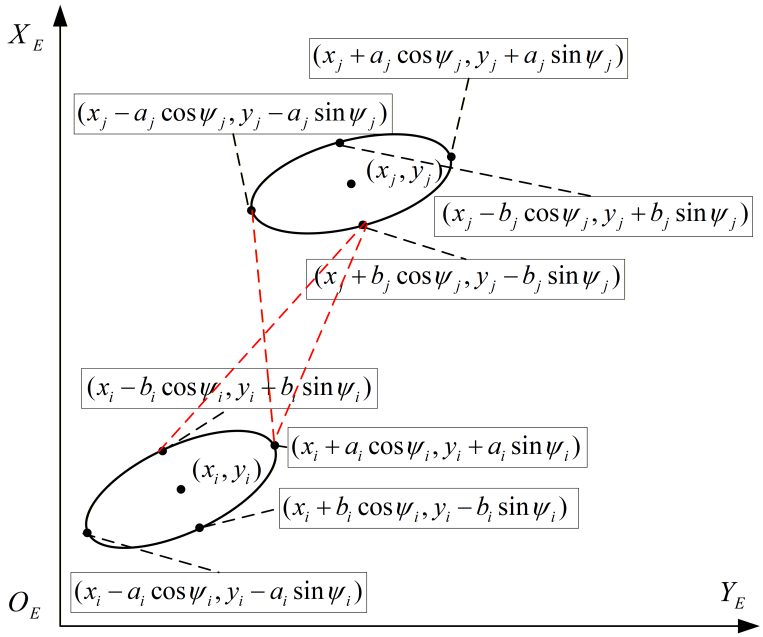


Figure 4. The generalized distance.

2.4. Obstacle Avoidance

Artificial potential functions (APFs) are widely used to incorporate obstacle avoidance into motion and formation control. Following common APF-based formulations [3,32], the kth static obstacle is modeled as a circular object surrounded by a repulsive potential field. The repulsive potential remains inactive when the ith USV is sufficiently far from the obstacle and increases as the USV approaches the prescribed safety boundary. Accordingly,

the repulsive potential function between the ith USV and the kth static obstacle is defined as follows:

$$p_{ik}^{o} = \begin{cases} \frac{\alpha_o (p_{ikv}^2 - \bar{p}_{ikv})^2}{2(p_{ikv}^2 - \underline{p}_{ikv})^2}, & \text{if } p_{ikv} \le \bar{R}_c \\ 0, & \text{otherwise} \end{cases} \tag{8}$$

where α_o is a positive constant, and $\bar{R}_o$ specifies the collision range associated with the obstacles. The relative-position vector between the ith USV and the kth obstacle is expressed as $p_{ik} = p_i - p_{ok}$, while its norm $p_{ikv} = \|p_{ik}\|$ $(k = 1, \ldots N_o)$ measures the corresponding separation distance.

2.5. Collision Avoidance

APF-based repulsive interactions have been widely used in distributed USV formation and swarm control to maintain inter-vessel separation [3,9,14,16,27]. In this paper, the inter-vessel repulsive potential is constructed using the proposed multi-point safety measure and is defined as follows:

$$p_{ij}^{c} = \begin{cases} \frac{\alpha_c (p_{ijv}^2 - \bar{p}_{ijv})^2}{2(p_{ijv}^2 - \underline{p}_{ijv})^2}, & \text{if } p_{ijv} \le \bar{R}_c \\ 0, & \text{otherwise} \end{cases} \tag{9}$$

where the relative-position vector is expressed as $p_{ij} = p_i - p_j$, and $p_{ijv} = \|p_{ij}\|$ gives the corresponding separation between the ith USV and the jth USV. The parameter $\bar{R}_c$ specifies the collision radius associated with the jth USV, whereas α_c is a positive constant.

2.6. Integrated Collision and Obstacle Avoidance Coordination

The control laws for the ith USV are constructed using a synthesized reference trajectory obtained by jointly considering the target position and the integrated potential fields for collision and obstacle avoidance. A coordination strategy is embedded in the resulting composite potential fields, whose mathematical form is given by

$$p_{ik}^{s} = \begin{bmatrix} \sum_{j=1}^{N} c_{ij}^{x} p_{ij}^{c} + \sum_{k=1}^{N_o} o_{ik}^{x} p_{ik}^{o} \\ \sum_{j=1}^{N} c_{ij}^{y} p_{ij}^{c} + \sum_{k=1}^{N_o} o_{ik}^{y} p_{ik}^{o} \end{bmatrix}. \tag{10}$$

where c_{ik}^{x}, c_{ik}^{y}, o_{ik}^{x} and o_{ik}^{y} specify the coordination directions adopted for collision and obstacle avoidance, with their expressions given by

$$\begin{cases} c_{ij}^{x} = \text{sign}(\partial p_{ik}^{c} / \partial x_i) \\ c_{ij}^{y} = \text{sign}(\partial p_{ij}^{c} / \partial y_i) \\ o_{ik}^{x} = \text{sign}(\partial p_{ik}^{o} / \partial x_i) \\ o_{ik}^{y} = \text{sign}(\partial p_{ik}^{o} / \partial y_i) \end{cases} \tag{11}$$

At each control update, the relative information of neighboring USVs and static obstacles is first used to evaluate the corresponding proximity measures. When a proximity measure enters its prescribed activation range, the associated repulsive potential is activated; otherwise, the corresponding potential term remains zero. The directional terms in Equation (11) determine the repulsive directions along the earth-fixed coordinates, and all active collision- and obstacle-avoidance terms are combined through Equation (10). The resulting avoidance term is then incorporated into the formation-error dynamics and subsequently affects the virtual and actual control inputs.

Incorporating the total potential fields into the formation task leads to the following control objective:

$$\lim_{t\to+\infty} \|p_i - p_j - p_{ij,d} - p_{ik}^s\| < c_0, \tag{12}$$

where $c_0 \in \mathbb{R}$ is selected as a small positive constant.

For $p_{ikv} \geq \bar{R}_o$, the APF remains inactive and the USV continues to maintain the prescribed formation $p_{ij,d}$, as indicated in Figure 2. The parameter o_{ik}, however, determines the encounter direction between the USV and obstacles.

3. Distributed Output Feedback Control Design

The overall procedure of the proposed distributed output feedback control method is summarized in Figure 5. The measured position–heading signals and control inputs are first processed by the RBFNN-based observer to estimate the unavailable velocity states and lumped unknown dynamics. Meanwhile, the inter-vessel and obstacle information is used to construct the collision- and obstacle-avoidance potential terms. These quantities are then incorporated into the formation-error dynamics and the recursive backstepping design. Dynamic-surface filters and auxiliary compensation dynamics are employed to avoid repeated differentiation and to address underactuation and actuator saturation, respectively. Finally, the surge force and yaw moment are generated and applied to each follower USV.

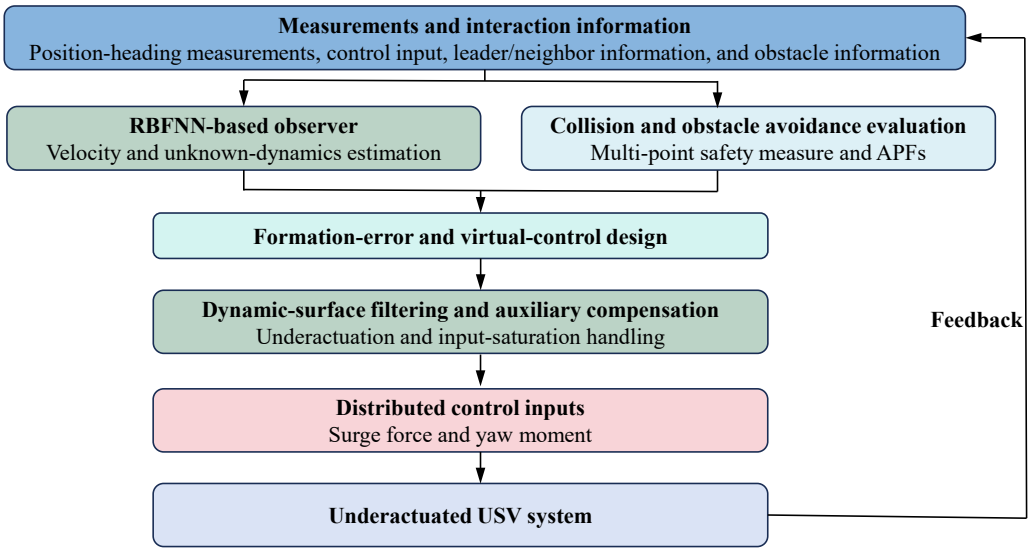


Figure 5. Flowchart of the proposed distributed output feedback formation-control method.

3.1. RBFNN-Based Observer Construction

Accurate modeling and output feedback control of underactuated USVs are often complicated by model uncertainties, unmodeled nonlinear dynamics, environmental disturbances, and unavailable velocity information [33,34]. Moreover, the relative configurations between neighboring vessels continuously vary during formation maneuvers, which further complicates an exact description of close-range interactions. In the present work, these uncertain single-vessel dynamic effects are treated as lumped unknown dynamics and are estimated by the proposed observer. Detailed near-field hydrodynamic coupling between neighboring vessel hulls is not explicitly modeled and is beyond the scope of this study. For observer design, the USV model in Equation (1) is rewritten as

$$\begin{aligned} \dot{\eta}_i &= J_i(\psi_i)\nu_i, \\ M_i\dot{\nu}_i &= \tau_i - \zeta_i, \end{aligned} \tag{13}$$

where the vectors are specified by $\eta_i = [x_i, y_i, \psi_i]^{\mathrm{T}}$ and $\nu_i = [u_i, v_i, r_i]^{\mathrm{T}}$. The model uncertainties and environmental disturbances are represented by $f_i = [f_{i,1}, f_{i,2}, f_{i,3}]^{\mathrm{T}}$ and $d_i = [d_{i,1}, d_{i,2}, d_{i,3}]^{\mathrm{T}}$, respectively, and their combined effect is expressed through $\zeta_i = [\zeta_{i,1}, \zeta_{i,2}, \zeta_{i,3}]^{\mathrm{T}} = -f_i - d_i$. The inertia properties of the ith USV are characterized by $M_i = \mathrm{diag}\{m_{i,11}, m_{i,22}, m_{i,33}\} \in \mathbb{R}^{3\times 3}$. The rotation matrix $J_i(\psi_i)$ takes the form

$$J_i(\psi_i) = \begin{bmatrix} \cos(\psi_i) & -\sin(\psi_i) & 0 \\ \sin(\psi_i) & \cos(\psi_i) & 0 \\ 0 & 0 & 1 \end{bmatrix}.$$

The universal approximation property of RBF neural networks over compact sets [28] enables the lumped unknown dynamics ζ_i to be approximated by a radial basis function neural network (RBFNN). Following the recorded input–output-data construction in [27,35], the control input τ_i and the current and delayed output signals of η_i are used as inputs to the RBFNN. Specifically,

$$\zeta_i = W_i^{\mathrm{T}} h_{ij}(\varsigma_i) + \varepsilon_i(\varsigma_i), \tag{14}$$

where the RBFNN input vector is constructed as $\varsigma_i = [\eta_i^{\mathrm{T}}, \eta_i^{\mathrm{T}}(t - t_d), \eta_i^{\mathrm{T}}(t - 2t_d), \tau_i^{\mathrm{T}}]^{\mathrm{T}}$, with $t_d > 0$. The basis-function vector satisfies $h_{ij}(\varsigma_i) \in \mathbb{R}^m$, where $j = 1, \ldots, m$ indexes the hidden-layer neurons. The weight matrix belongs to $W_i \in \mathbb{R}^{m\times 3}$. The approximation error is bounded according to $\|\varepsilon_i(\varsigma_i)\| \le \bar{\varepsilon}_i$, where $\bar{\varepsilon}_i$ is a positive constant.

Motivated by neural network-based output feedback observer designs for underactuated surface vessels [26,27], the RBFNN-based state observer is designed as follows:

$$\dot{\hat{\eta}}_i = J_i(\psi_i)\hat{v}_i - K_{oi1}\tilde{\eta}_i, \tag{15}$$

$$M_i\dot{\hat{v}}_i = \tau_i - \hat{W}_i^{\mathrm{T}} h_{ij}(\varsigma_i) - K_{oi2} J_i^{\mathrm{T}}(\psi_i)\tilde{\eta}_i, \tag{16}$$

where $K_{oi1}, K_{oi2} \in \mathbb{R}^{3\times 3}$ are selected as positive definite observer gain matrices. The state estimation error is expressed as $\tilde{\eta}_i = \hat{\eta}_i - \eta_i$, where the estimated state and velocity vectors are collected as $\hat{\eta}_i = [\hat{x}_i, \hat{y}_i, \hat{\psi}_i]^{\mathrm{T}}$ and $\hat{v}_i = [\hat{u}_i, \hat{v}_i, \hat{r}_i]^{\mathrm{T}}$, corresponding to the estimates of η_i and ν_i, respectively. The estimate associated with W_i is denoted by $\hat{W}_i$, whose adaptation rule is specified by

$$\dot{\hat{W}}_i = \gamma_i h_{ij}(\varsigma_i)\tilde{\eta}_i^{\mathrm{T}} J_i(\psi_i) - \rho_{i,w}\hat{W}_i, \tag{17}$$

where $\rho_{i,w}, \gamma_i \in \mathbb{R}$ are chosen as positive constants.

For clarity, the implementation procedure of the RBFNN-based observer is summarized in Algorithm 1. At each sampling instant, the measured position–heading signals, current observer estimates, and applied control input are used to construct the RBFNN input vector. The position–heading estimation error and RBF activation vectors are then evaluated to obtain the estimate of the lumped unknown dynamics. Subsequently, the position–heading estimates, velocity estimates, and adaptive neural-network weights are updated according to (15)–(17).

Algorithm 1 RBFNN-Based Observer for the ith USV

Input: measured position–heading η_i and applied control input τ_i
Initialization: $\hat{\eta}_i(0) = \eta_i(0)$, $\hat{v}_i(0) = 0$, and $\hat{W}_{i,q}(0) = 0$, $q = 1, 2, 3$
for each sampling instant t_k **do**
  Calculate the position–heading estimation error $\tilde{\eta}_i = \hat{\eta}_i - \eta_i$
  Construct the RBFNN input vector $\varsigma_i = [\eta_i^T, \hat{\eta}_i^T, \hat{v}_i^T, \tau_i^T]^T$
  Calculate the body-fixed estimation-error signal $\Delta_i = J_i^T(\psi_i)\tilde{\eta}_i$
  for $q = 1, 2, 3$ **do**
    for $j = 1, \ldots, m$ **do**
      Evaluate the RBF activation $h_{i,j,q}(\varsigma_i) = \exp\left(-\frac{\|\varsigma_i - c_{i,j,q}\mathbf{1}\|^2}{b_{i,q}^2}\right)$
    end for
    Define $h_{i,q} = [h_{i,1,q}, \ldots, h_{i,m,q}]^T$
    Estimate the qth component of the lumped unknown dynamics $\hat{\zeta}_{i,q} = \hat{W}_{i,q}^T h_{i,q}$
    Calculate the adaptive weight derivative $\dot{\hat{W}}_{i,q} = \gamma_{i,q} h_{i,q} \Delta_{i,q} - \rho_{i,q} \hat{W}_{i,q}$
    Update $\hat{W}_{i,q}(t_{k+1}) = \hat{W}_{i,q}(t_k) + T_s \dot{\hat{W}}_{i,q}(t_k)$
  end for
  Construct $\hat{\zeta}_i = [\hat{\zeta}_{i,1}, \hat{\zeta}_{i,2}, \hat{\zeta}_{i,3}]^T$
  Update $\hat{\eta}_i$ according to Equation (15)
  Update $\hat{v}_i$ according to Equation (16)
  Provide $\hat{v}_i$ and $\hat{\zeta}_i$ to the distributed controller
end for

For the subsequent control construction, the component forms of the relevant quantities are introduced as $\hat{W}_i = [\hat{W}_{1,i}, \hat{W}_{2,i}, \hat{W}_{3,i}]^{\mathrm{T}}$, $h_{ij}(\varsigma_i) = [h_{1,ij}(\varsigma_i), h_{2,ij}(\varsigma_i), h_{3,ij}(\varsigma_i)]^{\mathrm{T}}$, and $K_{oi2} = \mathrm{diag}\{K_{1,oi2}, K_{2,oi2}, K_{3,oi2}\}$. Accordingly, (16) can be written componentwise as

$$\dot{\hat{u}}_i = \frac{1}{m_{i,11}}(\tau_{i,u} - \hat{W}_{1,i} h_{1,ij}(\varsigma_i) - K_{1,oi2}\Delta_{1,i}), \tag{18}$$

$$\dot{\hat{v}}_i = \frac{1}{m_{i,22}}(-\hat{W}_{2,i} h_{2,ij}(\varsigma_i) - K_{2,oi2}\Delta_{2,i}), \tag{19}$$

$$\dot{\hat{r}}_i = \frac{1}{m_{i,33}}(\tau_{i,r} - \hat{W}_{3,i} h_{3,ij}(\varsigma_i) - K_{3,oi2}\Delta_{3,i}), \tag{20}$$

where the auxiliary terms are $\Delta_{1,i} = \cos(\psi_i)\tilde{x}_i + \sin(\psi_i)\tilde{y}_i$, $\Delta_{2,i} = -\sin(\psi_i)\tilde{x}_i + \cos(\psi_i)\tilde{y}_i$ and $\Delta_{3,i} = \tilde{\psi}_i$.

Using (15), (16), and (13) together yields the following observer error equations:

$$\dot{\tilde{\eta}}_i = J_i(\psi_i)\tilde{v}_i - K_{oi1}\tilde{\eta}_i, \tag{21}$$

$$M_i \dot{\tilde{v}}_i = -\tilde{W}_i^{\mathrm{T}} h_{ij}(\varsigma_i) + \varepsilon_i(\varsigma_i) - K_{oi2} J_i^{\mathrm{T}}(\psi_i)\tilde{\eta}_i, \tag{22}$$

where the velocity estimation error is expressed as $\tilde{v}_i = \hat{v}_i - v_i$.

For a compact representation, the observer errors are stacked into $X_i = [\tilde{\eta}_i^{\mathrm{T}}, \tilde{v}_i^{\mathrm{T}}]^{\mathrm{T}}$. Accordingly, (21) and (22) are written in matrix form as

$$\dot{X}_i = A_i X_i + B_i(-\tilde{W}_i^{\mathrm{T}} h_{ij}(\varsigma_i) + \varepsilon_i(\varsigma_i)), \tag{23}$$

$$\tilde{\eta}_i = C_{oi} X_i, \tag{24}$$

where

$$A_i = \begin{bmatrix} -K_{oi1} & J_i(\psi_i) \\ -M_i^{-1}K_{oi2}J_i^{\mathrm{T}}(\psi_i) & 0_3 \end{bmatrix}, B_i = \begin{bmatrix} 0_3 \\ M_i^{-1} \end{bmatrix},$$
$$C_{oi} = \begin{bmatrix} I_3 & 0_3 \end{bmatrix}.$$

Because A_i depends nonlinearly on $J_i(\psi_i)$, a direct stability analysis of the observer is difficult. Therefore, a change in coordinates is adopted according to $\chi_i = T_i X_i$, with $T_i = \mathrm{diag}\{J_i^{\mathrm{T}}(\psi_i), I_3\}$, yielding

$$\dot{\chi}_i = (A_{i0} + r_i S_T)\chi_i + B_i(-\tilde{W}_i^{\mathrm{T}} h_{ij}(\varsigma_i) + \varepsilon_i(\varsigma_i)), \tag{25}$$

where

$$A_{i0} = \begin{bmatrix} -K_{oi1} & I_3 \\ -M_i^{-1}K_{oi2} & 0_3 \end{bmatrix},$$

and $S_T = \mathrm{diag}\{S_1, I_3\}$ with

$$S_1 = \begin{bmatrix} 0 & 1 & 0 \\ -1 & 0 & 0 \\ 0 & 0 & 0 \end{bmatrix}.$$

Lemma 2. *If* $\frac{\rho_i}{2\gamma_i} - \frac{\bar{h}_{ij}^2}{2} > 0$ *and symmetric positive definite matrices* $Q_i, P_i \in \mathbb{R}^{6\times 6}$ *can be found such that the inequalities below are satisfied, then the observer estimation error* X_i *is bounded:*

$$\begin{aligned} &A_{i0}^{\mathrm{T}}P_i + P_iA_{i0} + P_iB_iB_i^{\mathrm{T}}P_i + Q_i \\ &\quad + F_iF_i^{\mathrm{T}} + \bar{r}_i(S_T^{\mathrm{T}}P_i + P_iS_T) \le 0, \end{aligned} \tag{26}$$

$$\begin{aligned} &A_{i0}^{\mathrm{T}}P_i + P_iA_{i0} + P_iB_iB_i^{\mathrm{T}}P_i + Q_i \\ &\quad + F_iF_i^{\mathrm{T}} - \bar{r}_i(S_T^{\mathrm{T}}P_i + P_iS_T) \le 0, \end{aligned} \tag{27}$$

where $F_i = C_{oi}^{\mathrm{T}} - P_iB_i$, *while* $\bar{r}_i \in \mathbb{R}$ *specifies an upper bound for* r_i.

Proof. The analysis is carried out using the Lyapunov function:

$$V_{io} = \frac{1}{2}\chi_i^{\mathrm{T}}P_i\chi_i + \frac{1}{2\gamma_i}\mathrm{tr}(\tilde{W}_i^{\mathrm{T}}\tilde{W}_i). \tag{28}$$

Taking the time derivative of V_{io} gives

$$\begin{aligned} \dot{V}_{io} =& \frac{1}{2}\chi_i^{\mathrm{T}}(P_iA_{i0} + A_{i0}^{\mathrm{T}}P_i + r_iP_iS_T + r_iS_T^{\mathrm{T}}P_i)\chi_i \\ &+ \chi_i^{\mathrm{T}}P_iB_i(-\tilde{W}_i^{\mathrm{T}}h_{ij}(\varsigma_i) + \varepsilon_i(\varsigma_i))) \\ &+ \frac{1}{\gamma_i}\mathrm{tr}(\tilde{W}_i^{\mathrm{T}}\dot{\tilde{W}}_i) \\ \le& \frac{1}{2}\chi_i^{\mathrm{T}}[P_iA_{i0} + A_{i0}^{\mathrm{T}}P_i + r_iP_iS_T + r_iS_T^{\mathrm{T}}P_i]\chi_i \\ &+ \chi_i^{\mathrm{T}}F_i\tilde{W}_i^{\mathrm{T}}h_{ij}(\varsigma_i) + \chi_i^{\mathrm{T}}P_iB_i\varepsilon_i(\varsigma_i) \\ &- \frac{\rho_i}{\gamma_i}\mathrm{tr}(\tilde{W}_i^{\mathrm{T}}\hat{W}_i). \end{aligned} \tag{29}$$

Observe that $-\mathrm{tr}(\tilde{W}_i^{\mathrm{T}}\hat{W}_i) \le -\frac{1}{2}\|\tilde{W}_i\|_F^2 + \frac{1}{2}\|W_i\|_F^2$, $-\chi_i^{\mathrm{T}}F_i\tilde{W}_i^{\mathrm{T}}h_{ij}(\varsigma_i) \le \frac{1}{2}\chi_i^{\mathrm{T}}F_iF_i^{\mathrm{T}}\chi_i + \frac{1}{2}\tilde{W}_i^{\mathrm{T}}h_{ij}(\varsigma_i)h_{ij}^{\mathrm{T}}(\varsigma_i)\tilde{W}_i$, and $\chi_i^{\mathrm{T}}P_iB_i\varepsilon_i(\varsigma_i) \le \frac{1}{2}\chi_i^{\mathrm{T}}P_iB_iB_i^{\mathrm{T}}P_i\chi_i + \frac{1}{2}\varepsilon_i^2(\varsigma_i)$, which yields

$$\begin{aligned}\dot{V}_{io} \leq & -\frac{\lambda_{\min}(Q_i)}{2}\|\chi_i\|^2 - (\frac{\rho_i}{2\gamma_i} - \frac{\bar{h}_{ij}^2}{2})\|\tilde{W}_i\|_F^2 \\ & + \frac{\rho_i}{2\gamma_i}\|W_i\|_F^2 + \frac{1}{2}\epsilon_i^2(\varsigma_i) \\ \leq & -c_{i2}V_{io} + c_{i1},\end{aligned} \tag{30}$$

where $c_{i1} = \frac{\rho_i}{2\gamma_i}\|W_i\|_F^2 + \frac{1}{2}\|\bar{\varepsilon}_i(\varsigma_i)\|^2$, $c_{i2} = \min\{\frac{\lambda_{\min}(Q_i)}{\lambda_{\max}(P_i)}, \rho_i - \gamma_i\bar{h}_{ij}^2\}$. Inequality (30) implies that the state χ_i remains bounded. Given that $T_i^{\mathrm{T}} = T_i^{-1}$ and $X_i = T_i^{\mathrm{T}}\chi_i$, the boundedness of the estimation error signal X_i is ensured. □

3.2. Controller Design

The subsequent control development employs the following representation of the kinematic model for the ith USV:

$$\dot{p}_i = R_i z_i, \tag{31}$$

$$\dot{\psi}_i = r_i, \tag{32}$$

where

$$R_i = \begin{bmatrix} \cos(\psi_i) & -\sin(\psi_i) \\ \sin(\psi_i) & \cos(\psi_i) \end{bmatrix},$$

$z_i = [u_i, v_i]^{\mathrm{T}}$.

The distributed formation controller is developed recursively using the backstepping methodology [36]. A stepwise design procedure is presented below.

Step 1: Based on the kinematics (31) and (32), modified error functions incorporating neighbors and obstacles information are defined as

$$\begin{aligned}p_{i,e} &= [p_{i,e1}, p_{i,e2}]^{\mathrm{T}} \\ &= R_i^{\mathrm{T}}[\sum_{j=0}^{n} a_{ij}(p_i - p_j - p_{ij,d} - \bar{p}_{ik}^s)].\end{aligned} \tag{33}$$

where $a_{ij} = 1$ indicates that the ith USV has access to the position information of the jth USV; in the absence of such information, $a_{ij} = 0$.

Differentiating $p_{i,e}$ and using (31) yields

$$\begin{aligned}\dot{p}_{i,e} = & -r_i S p_{i,e} + a_{s,i} z_i - R_i^{\mathrm{T}} a_{s,i} R_j z_j \\ & - R_i^{\mathrm{T}} a_{s,i}(\dot{p}_{ij,d} + \dot{\bar{p}}_{ik}^s),\end{aligned} \tag{34}$$

where $a_{s,i} = \sum_{j=0}^{n} a_{ij}$,

$$S = \begin{bmatrix} 0 & 1 \\ -1 & 0 \end{bmatrix}.$$

The vector $\beta_i = [\beta_{i,1}, \beta_{i,2}]^{\mathrm{T}}$ is introduced as the virtual input associated with (34). Accordingly, β_i is selected at the kinematic level according to

$$\beta_i = [-K_{i,1}p_{i,e} + R_i^{\mathrm{T}} a_{s,i} R_j \hat{z}_j + R_i^{\mathrm{T}} a_{s,i}(\dot{p}_{ij,d} + \dot{\bar{p}}_{ik}^s)]/a_{s,i}, \tag{35}$$

with $K_{i,1} \in \mathbb{R}^{2\times 2}$ chosen to be diagonal.

Introduce $\tilde{p}_{ik} = \dot{p}_{ik}^{f} - \dot{p}_{ik}^{s}$. Since R_i, $a_{s,i}$ and $\tilde{p}_{ik}$ are bounded, a positive constant μ_1 can be selected such that $\sum_{i=1}^{n} \| R_i^{\mathrm{T}} a_{s,i} \tilde{p}_{ik} \| \leq \mu_1$.

Step 2: The next error variable is introduced as

$$\psi_{i,e} = \psi_i - \psi_{i,a}, \tag{36}$$

The line-of-sight (LOS) guidance law [27,37,38] is employed to determine the desired heading angle $\psi_{i,a}$ as

$$\psi_{i,a} = \psi_j - f, \tag{37}$$

$$f = \mathrm{atan}(\hat{v}_i / \hat{u}_j) - \mathrm{atan}(p_{ie2} / \Delta), \tag{38}$$

where $\Delta > 0$ denotes the LOS look-ahead parameter. In the numerical implementation, follower-dependent look-ahead parameters are adopted, and their values are summarized in Table 1.

Table 1. Main settings of the simulation environment.

Item	Setting
Simulation platform	MATLAB R2022b
Simulation horizon	300 s
Numerical step	0.01 s
Integration method for USV dynamics	Classical fourth-order Runge–Kutta (RK4)
Formation system	One virtual leader and four follower USVs
Vessel model	CyberShip II
Observer gains	$K_{oi1} = K_{oi2} = 30 I_3$
RBFNN hidden nodes	9
RBFNN adaptation gain	1000
RBFNN leakage coefficient	0.1
Initial RBFNN weights	$\hat{W}_i(0) = 0_{9\times 3}$
Controller gains	$K_{i,1} = \mathrm{diag}\{4,4\}$, $k_{i,2} = 4$, $k_{i,3} = 20$, $k_{i,4} = 0.5$, $k_{i,5} = 12$
Auxiliary-compensation parameters	$T_u = 10$, $T_r = 20$, $\gamma_1 = 20$
Dynamic-surface-filter constants	$l_{i,1} = l_{i,2} = l_{i,3} = 0.1$
External disturbance	Bounded deterministic sinusoidal disturbance
Disturbance bounds	$\lvert d_{i,u} \rvert \leq 0.48$ N, $\lvert d_{i,v} \rvert \leq 0.44$ N, $\lvert d_{i,r} \rvert \leq 0.491$ N·m
Surge-force constraint	$[-2, 2]$ N
Yaw-moment constraint	$[-1.5, 1.5]$ N·m
Static-obstacle centers	$[20, 3]^T$ m and $[20, -3]^T$ m
Static-obstacle radius	2 m
Ellipse semi-major axis	0.75 m
Ellipse semi-minor axis	0.35 m
RBFNN basis-function widths	$b_{i,1} = b_{i,2} = b_{i,3} = 30$
LOS look-ahead parameters	$\Delta_1 = 1$ m, $\Delta_2 = 0.3$ m, $\Delta_3 = 0.5$ m; $\Delta_4 = 0.2$ m for $t \leq 150$ s and $\Delta_4 = 0.5$ m for $t > 150$ s

Differentiating $\psi_{i,e}$ and using (32) yields

$$\dot{\psi}_{i,e} = r_i - \dot{\psi}_{i,a}. \tag{39}$$

For the controller design, the stabilizing function $\beta_{i,3}$ is selected in the following form:

$$\beta_{i,3} = -k_{i,2} \psi_{i,e} + \hat{z}_j + \dot{f}, \tag{40}$$

Here, $k_{i,2}$ represents a positive constant.

Step 3: Introduce the velocity errors as

$$u_{i,e} = \hat{u}_i - \bar{\beta}_{i,1} - \gamma_1 \tanh(\alpha_{i,1}), \tag{41}$$

$$v_{i,e} = \hat{v}_i - \bar{\beta}_{i,2} - \tanh(\alpha_{i,2}), \tag{42}$$

$$r_{i,e} = \hat{r}_i - \bar{\beta}_{i,3} - \gamma_1 \tanh(\alpha_{i,3}), \tag{43}$$

where γ_1 is a positive constant, and $\alpha_{i,h}$ $(h = 1,2,3)$ denotes an auxiliary control term introduced to address the underactuated nature and input saturation. To avoid the repeated differentiation of virtual control laws in the backstepping procedure, a first-order dynamic-surface filter [39] is introduced: $l_{i,h}\dot{\bar{\beta}}_{i,h} + \bar{\beta}_{i,h} = \beta_{i,h}$, $h = 1,2,3$, where $l_{i,h}$ is set to a positive filter constant.

Differentiating (41)–(43) and substituting (18)–(20) yields

$$\begin{aligned} \dot{u}_{i,e} = {} & \frac{1}{m_{i,11}}[\tau_{i,uc} - \varpi_{i,u} - \hat{W}_{1,i}h_{1,ij}(\varsigma_i) - K_{1,oi2}\Delta_{1,i}] \\ & - \dot{\bar{\beta}}_{i,1} - \gamma_1 \frac{\dot{\alpha}_{i,1}}{\cosh^2(\alpha_{i,1})}, \end{aligned} \tag{44}$$

$$\begin{aligned} \dot{v}_{i,e} = {} & \frac{1}{m_{i,22}}[-\hat{W}_{2,i}h_{2,ij}(\varsigma_i) - K_{2,oi2}\Delta_{2,i}] - \dot{\bar{\beta}}_{i,2} \\ & - \frac{\dot{\alpha}_{i,2}}{\cosh^2(\alpha_{i,2})}, \end{aligned} \tag{45}$$

$$\begin{aligned} \dot{r}_{i,e} = {} & \frac{1}{m_{i,33}}[\tau_{i,rc} - \varpi_{i,r} - \hat{W}_{3,i}h_{3,ij}(\varsigma_i) - K_{3,oi2}\Delta_{3,i}] \\ & - \dot{\bar{\beta}}_{i,3} - \gamma_1 \frac{\dot{\alpha}_{i,3}}{\cosh^2(\alpha_{i,3})}. \end{aligned} \tag{46}$$

Following the auxiliary compensation structure in [27], the update laws used to address underactuation and actuator saturation are given by

$$\dot{\alpha}_{i,1} = \cosh^2(\alpha_{i,1})(-T_u\alpha_{i,1} - \varpi_{i,u}/m_{i,11})/\gamma_1, \tag{47}$$

$$\begin{aligned} \dot{\alpha}_{i,2} = {} & \cosh^2(\alpha_{i,2})\{-\hat{W}_{2,i}h_{2,ij}(\varsigma_i)/m_{i,22} + k_{i,4}v_{i,e} \\ & + a_{s,i}p_{i,e2} - \dot{\bar{\beta}}_{i,2}\}, \end{aligned} \tag{48}$$

$$\dot{\alpha}_{i,3} = \cosh^2(\alpha_{i,3})(-T_r\alpha_{i,3} - \varpi_{i,r}/m_{i,33})/\gamma_1, \tag{49}$$

The parameters $k_{i,4}$, T_u and T_r are chosen as positive constants.

Step 4: The kinetic control laws for stabilizing the system are formulated as

$$\begin{aligned} \tau_{i,uc} = {} & m_{i,11}(-k_{i,3}u_{i,e} - T_u\alpha_{i,1} + \dot{\bar{\beta}}_{i,1} - a_{s,i}p_{i,e1}) \\ & + \hat{W}_{1,i}h_{1,ij}(\varsigma_i), \end{aligned} \tag{50}$$

$$\tau_{i,rc} = m_{i,33}(-k_{i,5}r_{i,e} + \dot{\bar{\beta}}_{i,3} - T_r\alpha_{i,3} - \psi_{i,e}) + \hat{W}_{3,i}h_{3,ij}(\varsigma_i). \tag{51}$$

Theorem 1. *For a system of N USVs affected by input saturation, suppose that the distributed control laws (50) and (51), the observer described by (15) and (16), and the auxiliary control terms (47)–(49) are implemented. With the proposed output feedback control scheme, every error signal of the resulting closed-loop system is bounded.*

Proof. A composite Lyapunov function is selected to simultaneously characterize the formation-position error, heading error, velocity errors, dynamic-surface-filter errors, observer estimation error, and the collision/obstacle-avoidance potential term. This structure is consistent with the recursive backstepping and observer-based design and facilitates the treatment of the coupling and cross terms among the corresponding subsystems. Accordingly, the Lyapunov function is defined as follows:

$$V = \sum_{i=1}^{n}(\frac{1}{2}p_{i,e}^{\mathrm{T}}p_{i,e} + \frac{1}{2}\psi_{i,e}^2 + \frac{1}{2}u_{i,e}^2 + \frac{1}{2}v_{i,e}^2 + \frac{1}{2}r_{i,e}^2 + \sum_{h=1}^{3}\omega_{i,h}^2 + V_{io} + p_{ik}) \tag{52}$$

For $h = 1, 2, 3$, $\omega_{i,h}$ represents the discrepancy between $\bar{\beta}_{i,h}$ and $\beta_{i,h}$ and is written as:

$$\omega_{i,1} = \bar{\beta}_{i,1} - \beta_{i,1}, \tag{53}$$

$$\omega_{i,2} = \bar{\beta}_{i,2} - \beta_{i,2}, \tag{54}$$

$$\omega_{i,3} = \bar{\beta}_{i,3} - \beta_{i,3}. \tag{55}$$

Differentiating V along (30), (34), (39), and (44)–(46) generates

$$\begin{aligned}\dot{V} = \sum_{i=1}^{n}\big(&p_{i,e}^{\mathrm{T}}[a_{s,i}(z_{i,e} + \beta_i + \omega_i + \bar{\alpha} - \tilde{z}_i) - R_i^{\mathrm{T}}a_{s,i}R_jz_j \\ &- R_i^{\mathrm{T}}a_{s,i}(\dot{p}_{ij,d} + \bar{p}_{ik}^{c})] + \psi_{i,e}(r_i - \dot{\psi}_{i,a}) \\ &+ u_{i,e}\{\frac{1}{m_{i,11}}[\tau_{i,uc} - \varpi_{i,u} - \hat{W}_{1,i}h_{1,ij}(\varsigma_i) \\ &- K_{1,oi2}\Delta_{1,i}] - \dot{\bar{\beta}}_{i,1} - \gamma_1\frac{\dot{\alpha}_{i,1}}{\cosh^2(\alpha_{i,1})}\} \\ &+ v_{i,e}\{\frac{1}{m_{i,22}}[-\hat{W}_{2,i}h_{2,ij}(\varsigma_i) - K_{2,oi2}\Delta_{2,i}] - \dot{\bar{\beta}}_{i,2} \\ &- \frac{\dot{\alpha}_{i,2}}{\cosh^2(\alpha_{i,2})}\} + r_{i,e}\{\frac{1}{m_{i,33}}[\tau_{i,rc} - \varpi_{i,r} \\ &- \hat{W}_{3,i}h_{3,ij}(\varsigma_i) - K_{3,oi2}\Delta_{3,i}] - \dot{\bar{\beta}}_{i,3} \\ &- \gamma_1\frac{\dot{\alpha}_{i,3}}{\cosh^2(\alpha_{i,3})}\} + \sum_{h=1}^{3}\omega_{i,h}(\dot{\bar{\beta}}_{i,h} - \dot{\beta}_{i,h}) \\ &- \lambda_{\min}(Q_i)\|\chi_i\|^2 - (\frac{\rho_i}{2\gamma_i} - \frac{\bar{h}_{ij}^2}{2})\|\tilde{W}_i\|_F^2 + c_{i1} + \dot{p}_{ik}\big).\end{aligned} \tag{56}$$

Moreover, substituting the virtual controls (35), (40), update laws for the auxiliary controls (47)–(49), and control laws (50) and (51) into (56), we obtain

$$\begin{aligned}\dot{V} \leq \sum_{i=1}^{n}\{&-\lambda_{\min}(K_{i,1})p_{i,e}^{\mathrm{T}}p_{i,e} - k_{i,2}\psi_{i,e}^2 \\ &+ p_{i,e}^{\mathrm{T}}a_{s,i}(\omega_i + \bar{\alpha} - \tilde{z}_i) + p_{i,e}^{\mathrm{T}}R_i a_{s,i}R_j^{\mathrm{T}}\tilde{z}_j + \psi_{i,e}(\omega_{i,3} + \tilde{r}_j - \tilde{r}_i) \\ &- k_{i,3}u_{i,e}^2 - k_{i,4}v_{i,e}^2 - k_{i,5}r_{i,e}^2 - \frac{K_{1,oi2}}{m_{i,11}}\Delta_{1,i}u_{i,e} \\ &- \frac{K_{2,oi2}}{m_{i,22}}\Delta_{2,i}v_{i,e} - \frac{K_{3,oi2}}{m_{i,33}}\Delta_{3,i}r_{i,e} \\ &- \sum_{h=1}^{3}\omega_{i,h}(\frac{\omega_{i,h}}{l_{i,h}} + \dot{\beta}_{i,h}) - \lambda_{\min}(Q_i)\|\chi_i\|^2 \\ &- (\frac{\rho_i}{2\gamma_i} - \frac{\bar{h}_{ij}^2}{2})\|\tilde{W}_i\|_F^2 + c_{i1} + \dot{p}_{ik}\}\end{aligned} \tag{57}$$

Here, $\hat{z}_i = [\hat{u}_i, \hat{v}_i]^{\mathrm{T}}$, while $\tilde{z}_i = \hat{z}_i - z_i$ and $\tilde{r}_i = \hat{r}_i - r_i$. From $l_{i,h}\dot{\bar{\beta}}_{i,h} + \bar{\beta}_{i,h} = \beta_{i,h}$, it follows that $\dot{\bar{\beta}}_{i,h} - \dot{\beta}_{i,h} = \frac{\beta_{i,h} - \bar{\beta}_{i,h}}{l_{i,h}} - \dot{\beta}_{i,h} = -\frac{\omega_{i,h}}{l_{i,h}} - \dot{\beta}_{i,h}$. In addition, $\omega_{i,h}(\frac{\omega_{i,h}}{l_{i,h}} + \dot{\beta}_{i,h})$ can be absorbed into $p_{i,e}^{\mathrm{T}}a_{s,i}\omega_i$ and $\psi_{i,e}\omega_{i,3}$,

$$\begin{aligned}\dot{V} \leq \sum_{i=1}^{n}\{&-\lambda_{\min}(K_{i,1})p_{i,e}^{\mathrm{T}}p_{i,e} - k_{i,2}\psi_{i,e}^2 \\ &+ p_{i,e}^{\mathrm{T}}a_{s,i}(\bar{\alpha} - \tilde{z}_i) + p_{i,e}^{\mathrm{T}}R_i a_{s,i}R_j^{\mathrm{T}}\tilde{z}_j + \psi_{i,e}(\tilde{r}_j - \tilde{r}_i) \\ &- k_{i,3}u_{i,e}^2 - k_{i,4}v_{i,e}^2 - k_{i,5}r_{i,e}^2 - \frac{K_{1,oi2}}{m_{i,11}}\Delta_{1,i}u_{i,e} \\ &- \frac{K_{2,oi2}}{m_{i,22}}\Delta_{2,i}v_{i,e} - \frac{K_{3,oi2}}{m_{i,33}}\Delta_{3,i}r_{i,e} \\ &- \sum_{h=1}^{3}(\frac{\omega_{i,h}^2}{l_{i,h}} - \frac{\omega_{i,h}^2\Omega_{i,h}^2}{2\varrho_i}) - \lambda_{\min}(Q_i)\|\chi_i\|^2 \\ &- (\frac{\rho_i}{2\gamma_i} - \frac{\bar{h}_{ij}^2}{2})\|\tilde{W}_i\|_F^2 + \frac{3\varrho_i}{2} + c_{i1} + \dot{p}_{ik}\}\end{aligned} \tag{58}$$

For subsequent analysis, introduce $\Omega_{i,1} = a_{s,i}p_{i,e1} - \dot{\beta}_{i,1}$, $\Omega_{i,2} = a_{s,i}p_{i,e2} - \dot{\beta}_{i,2}$ and $\Omega_{i,3} = \psi_{i,e} + \dot{\beta}_{i,3}$. Applying Young's inequality gives, for any $\varrho_i > 0$, $\omega_{i,h}\Omega_{i,h} \leq \frac{1}{2\varrho_i}\omega_{i,h}^2\Omega_{i,h}^2 + \frac{\varrho_i}{2}$. Next, consider the sets $\prod_i := \{\sum_{j=1}^{i} p_{j,e}^{\mathrm{T}}p_{j,e} + \psi_{j,e}^2 + u_{j,e}^2 + v_{j,e}^2 + r_{j,e}^2 + \sum_{h=1}^{3}\omega_{j,h}^2 + \tilde{X}_j^{\mathrm{T}}\tilde{X}_j + \frac{1}{\gamma_i}\mathrm{tr}(\tilde{W}_i^{\mathrm{T}}\tilde{W}_i) \leq 2\rho_\rho\}$ and $O_o := \{\eta_0^{\mathrm{T}}\eta_0 + \dot{\eta}_0^{T}\dot{\eta}_0 \leq \eta_0^{*}\}$, where ρ_ρ and η_0^* denote positive constants. Since $\prod_i \times O_o$ is compact in $\mathbb{R}^{18i+6}$, a positive constant $s_{i,h}$ can be selected such that $|\Omega_{i,h}| \leq s_{i,h}$ throughout this set.

To simplify the subsequent design, define $\bar{K}_{1o} = \frac{K_{1,oi2}}{m_{i,11}}$, $\bar{K}_{2o} = \frac{K_{2,oi2}}{m_{i,22}}$, $\bar{K}_{3o} = \frac{K_{3,oi2}}{m_{i,33}}$ and $\mu_1 = \sum_{i=1}^{n}(c_{i1} + \frac{3\varrho_i}{2} + \dot{p}_{ik})$. By Young's inequality, it holds that

$$p_{i,e}^{\mathrm{T}}a_{s,i}(\bar{\alpha} - \tilde{z}_i) \leq a_{s,i}(p_{i,e}^{\mathrm{T}}p_{i,e} + \frac{1}{2} + \frac{1}{2}\tilde{z}_i^{\mathrm{T}}\tilde{z}_i), \tag{59}$$

$$p_{i,e}^{\mathrm{T}}R_i a_{s,i}R_j^{\mathrm{T}}\tilde{z}_j \leq \frac{a_{s,i}}{2}(p_{i,e}^{\mathrm{T}}p_{i,e} + \tilde{z}_j^{\mathrm{T}}\tilde{z}_j), \tag{60}$$

$$\psi_{i,e}(\tilde{r}_j - \tilde{r}_i) \leq \psi_{i,e}^2 + \frac{1}{2}\tilde{r}_i^2 + \frac{1}{2}\tilde{r}_j^2, \tag{61}$$

$$\begin{aligned}\bar{K}_{1o}\Delta_{1,i}u_{ie} \leq & \bar{K}_{1o}u_{ie}(|\tilde{x}_i| + |\tilde{y}_i|) \\ \leq & \frac{\bar{K}_{1o}}{2}\tilde{x}_i^2 + \frac{\bar{K}_{1o}}{2}\tilde{y}_i^2 + \bar{K}_{1o}u_{ie}^2 \end{aligned} \tag{62}$$

$$\begin{aligned}\bar{K}_{2o}\Delta_{2,i}v_{ie} \leq & \bar{K}_{2o}v_{ie}(|\tilde{x}_i| + |\tilde{y}_i|) \\ \leq & \frac{\bar{K}_{2o}}{2}\tilde{x}_i^2 + \frac{\bar{K}_{2o}}{2}\tilde{y}_i^2 + \bar{K}_{2o}v_{ie}^2 \end{aligned} \tag{63}$$

$$\begin{aligned}\bar{K}_{3o}\Delta_{3,i}r_{ie} = & \bar{K}_{3o}\tilde{\psi}_i r_{ie} \\ \leq & \frac{\bar{K}_{3o}}{2}\tilde{\psi}_i^2 + \bar{K}_{3o}r_{ie}^2. \end{aligned} \tag{64}$$

Substituting (59)–(64) and $X_i = T_i^{\mathrm{T}}\chi_i$ into (58), we obtain

$$\begin{aligned}\dot{V} \leq \sum_{i=1}^{n}\{ & -[\lambda_{\min}(K_{i,1}) - \frac{3a_{s,i}}{2}]p_{i,e}^{\mathrm{T}}p_{i,e} - (k_{i,2}-1)\psi_{i,e}^2 \\ & - (k_{i,3} - \bar{K}_{1o})u_{i,e}^2 - (k_{i,4} - \bar{K}_{2o})v_{i,e}^2 \\ & - (k_{i,5} - \bar{K}_{3o})r_{i,e}^2 - \sum_{h=1}^{3}(\frac{\omega_{i,h}^2}{l_{i,h}} - \frac{\omega_{i,h}^2\Omega_{i,h}^2}{2\varrho_i}) \\ & - [\lambda_{\min}(Q_i) - \lambda_{ko}]\|\chi_i\|^2 - (\frac{\rho_i}{2\gamma_i} - \frac{\bar{h}_{ij}^2}{2})\|\tilde{W}_i\|_F^2 \\ & + \frac{a_{s,i}}{2}\} + \mu_1, \end{aligned} \tag{65}$$

where $\lambda_{ko} = \max\{\frac{\bar{K}_{1o}+\bar{K}_{2o}}{2}, \frac{\bar{K}_{3o}}{2}, a_{s,i}, 1\}$.

By selecting $1/l_{i,h} = s_{i,h}^2/(2\varrho_i) + l_{i,h}^*$, where $l_{i,h}^*$ is a positive constant, the following result is obtained:

$$\begin{aligned}\dot{V} \leq \sum_{i=1}^{n}\{ & -[\lambda_{\min}(K_{i,1}) - \frac{3a_{s,i}}{2}]p_{i,e}^{\mathrm{T}}p_{i,e} - (k_{i,2}-1)\psi_{i,e}^2 \\ & - (k_{i,3} - \bar{K}_{1o})u_{i,e}^2 - (k_{i,4} - \bar{K}_{2o})v_{i,e}^2 - (k_{i,5} - \bar{K}_{3o})r_{i,e}^2 \\ & - \sum_{h=1}^{3} l_{i,h}^*\omega_{i,h}^2 - \sum_{h=1}^{3}(1 - \frac{\Omega_{i,h}^2}{s_{i,h}^2})\frac{\omega_{i,h}^2 s_{i,h}^2}{2\varrho_i} \\ & - [\lambda_{\min}(Q_i) - \lambda_{ko}]\|\chi_i\|^2 - (\frac{\rho_i}{2\gamma_i} - \frac{\bar{h}_{ij}^2}{2})\|\tilde{W}_i\|_F^2\} \\ & + \mu_2, \end{aligned} \tag{66}$$

where $\mu_2 = \mu_1 + \sum_{i=1}^{n}\frac{a_{s,i}}{2}$.

Substituting the bound $|\Omega_{i,h}| \leq s_{i,h}$ into (66) yields

$$\dot{V} \leq -\mu_0 V + \mu_2, \tag{67}$$

where $\mu_0 = \min\{2[\lambda_{\min}(K_{1,i}) - \frac{3a_{s,i}}{2}], 2(k_{i,2}-1), 2(k_{i,3} - \bar{K}_{1o}), 2(k_{i,4} - \bar{K}_{2o}), 2(k_{i,5} - \bar{K}_{3o}), 2l_{i,h}^*, 2[\lambda_{\min}(Q_i) - \lambda_{ko}], (\frac{\rho_i}{\gamma_i} - \bar{h}_{ij}^2)\}$.

Hence,

$$V(t) \leq (V(0) - \frac{\mu_2}{\mu_0})e^{-\mu_0 t} + \frac{\mu_2}{\mu_0}. \tag{68}$$

The definition of V implies the boundedness of every error signal in the closed-loop system. □

4. Simulation Results

4.1. Simulation Environment and Setup

All numerical simulations were implemented in MATLAB R2022b with a fixed numerical step of 0.01 s over a simulation horizon of 300 s. The kinematic and dynamic equations of the USVs were numerically integrated using the classical fourth-order Runge–Kutta (RK4) method, while the controller and observer states were updated at the same sampling interval. A formation system consisting of one virtual leader and four follower USVs was considered to evaluate the proposed control strategy. Under the directed spanning-tree condition in Assumption 1, a single rooted leader is sufficient to propagate the reference information to all follower USVs [7–9]. Introducing multiple leaders would instead lead to a multi-leader or containment-control formulation [33], which is beyond the formation-tracking objective considered in this study.

The vessel model and its principal parameters were based on the CyberShip II model ship developed at the Norwegian University of Science and Technology [40]. CyberShip II is adopted as a benchmark model because its dynamic parameters are well documented and have been widely used in marine-control studies, which facilitates reproducible controller evaluation and comparison with related work. The proposed control framework is not restricted to this specific platform and can be applied to other underactuated USV models satisfying the stated assumptions after replacing the corresponding vessel parameters. The simulation configuration, including the initial positions of the virtual leader and follower USVs, the locations of the two static obstacles, and the leader-motion direction, is illustrated in Figure 6. The main simulation settings are summarized in Table 1.

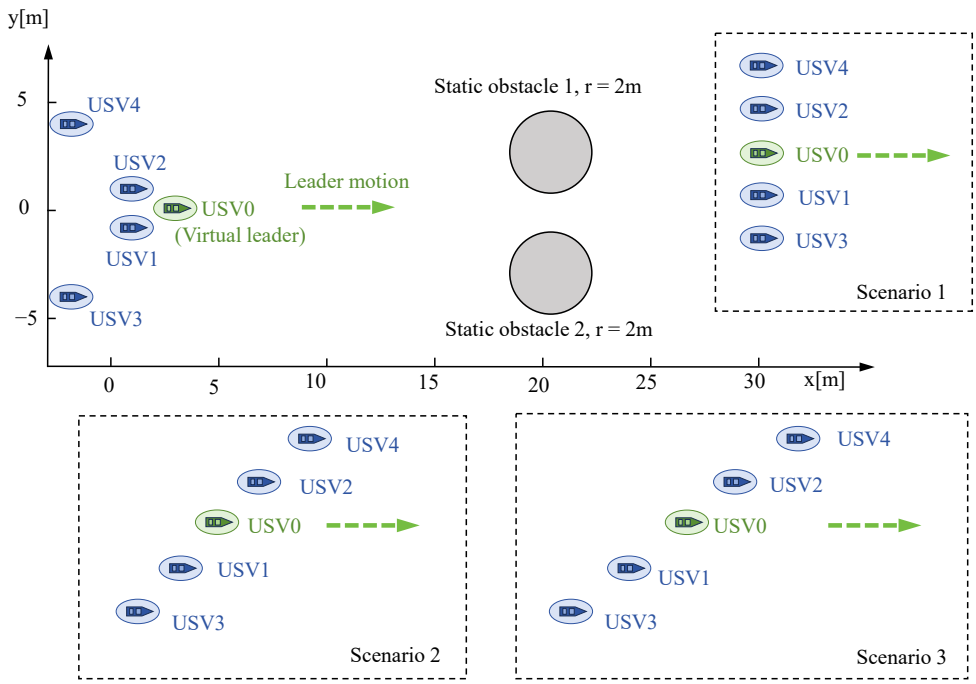


Figure 6. Initial simulation configuration of the case study.

Neural network-based observer schemes have been employed to compensate for uncertain dynamics in underactuated surface vessels [26,27,34]. In the present work, the RBFNN is used specifically as an online function approximator within the state observer to estimate the lumped unknown dynamics, rather than as an independent high-level

decision-making controller. Its principal implementation parameters are summarized in Table 1.

The inertia and damping matrices used for all follower USVs are

$$M_i = \mathrm{diag}\{23.8,\ 33.8,\ 2.764\}, \qquad D_i = \begin{bmatrix} 2 & 0 & 0 \\ 0 & 7 & 0.1 \\ 0 & 0.1 & 0.5 \end{bmatrix}.$$

The virtual leader starts from $\eta_0(0) = [2.6\ \mathrm{m},\ 0\ \mathrm{m},\ 0\ \mathrm{rad}]^T$ and moves with constant velocities $u_0 = 0.1$ m/s, $v_0 = 0$ m/s, and $r_0 = 0$ rad/s throughout the simulation. Accordingly, its reference trajectory over the considered 300-s simulation interval is

$$x_0(t) = 2.6 + 0.1t, \qquad y_0(t) = 0, \qquad \psi_0(t) = 0.$$

The initial position and heading vectors of the follower USVs are selected as

$$\eta_1(0) = [1\ \mathrm{m},\ 1\ \mathrm{m},\ 0\ \mathrm{rad}]^T, \qquad \eta_2(0) = [1\ \mathrm{m},\ -1\ \mathrm{m},\ 0\ \mathrm{rad}]^T,$$

$$\eta_3(0) = [-2\ \mathrm{m},\ 4\ \mathrm{m},\ 0\ \mathrm{rad}]^T, \qquad \eta_4(0) = [-2\ \mathrm{m},\ -4\ \mathrm{m},\ 0\ \mathrm{rad}]^T.$$

The initial velocities of all follower USVs are set to zero, i.e., $\nu_i(0) = 0_3$, $i = 1, \ldots, 4$. The initial position–heading estimates are set equal to the corresponding actual states, while the initial estimated velocities and RBFNN weights are selected as

$$\hat{\eta}_i(0) = \eta_i(0), \qquad \hat{\nu}_i(0) = 0_3, \qquad \hat{W}_i(0) = 0_{9\times 3}, \quad i = 1, \ldots, 4.$$

The observer, RBFNN, controller, auxiliary-compensation, dynamic-surface-filter, and LOS-guidance parameters are summarized in Table 1. Unless otherwise specified, the same parameter values are used for all four follower USVs and throughout the three simulation scenarios. The follower-dependent LOS look-ahead parameters are explicitly listed in Table 1.

To evaluate the robustness of the observer and controller, bounded deterministic time-varying disturbances are applied to all follower USVs. The disturbance vector is selected as

$$d_i(t) = \begin{bmatrix} -0.13 - 0.20\sin(0.12t) - 0.15\sin(0.06t) \\ 0.09 - 0.20\sin(0.08t - \pi/6) - 0.15\sin(0.06t) \\ 0.10\sin(0.09 + \pi/3) + 0.40\sin(0.05t) \end{bmatrix}, \qquad i = 1, \ldots, 4,$$

where the first two components represent generalized disturbance forces in N, whereas the third component represents a disturbance yaw moment in N·m. Accordingly, the disturbance components satisfy the conservative bounds

$$|d_{i,u}(t)| \le 0.48\ \mathrm{N}, \qquad |d_{i,v}(t)| \le 0.44\ \mathrm{N}, \qquad |d_{i,r}(t)| \le 0.491\ \mathrm{N\cdot m}.$$

The same disturbance signals are applied to all follower USVs and are used consistently in the proposed and comparative simulations.

The surge forces and yaw moments are constrained by $|\tau_{i,u}| \le 2$ N and $|\tau_{i,r}| \le 1.5$ N·m, respectively.

Two circular static obstacles, each with a radius of 2 m, are centered at $[20\ \mathrm{m},\ 3\ \mathrm{m}]^T$ and $[20\ \mathrm{m},\ -3\ \mathrm{m}]^T$. For the proposed multi-point safety measure, the same virtual elliptical reference geometry is assigned to all follower USVs, with the semi-major and semi-minor axes selected as

$$a_i = 0.75\ \mathrm{m}, \qquad b_i = 0.35\ \mathrm{m}, \qquad i = 1, \ldots, 4.$$

These parameters are used to determine the locations of the four characteristic safety points and are not intended to provide an exact geometric reconstruction of the CyberShip II hull.

The initial simulation configuration considered in the case study is illustrated in Figure 6. The figure shows the initial positions and headings of the virtual leader and four follower USVs, the locations and sizes of the two static obstacles, and the motion direction of the virtual leader. This configuration is used as the common initial environment for the comparative simulation scenarios considered below.

Six simulations are conducted under three desired formation geometries. In Scenario 1, the desired relative-position offsets are

$$p_{10,d} = [0\ \mathrm{m}, -4\ \mathrm{m}]^{\mathrm{T}}, \qquad p_{20,d} = [0\ \mathrm{m}, 4\ \mathrm{m}]^{\mathrm{T}},$$

$$p_{31,d} = [0\ \mathrm{m}, -4\ \mathrm{m}]^{\mathrm{T}}, \qquad p_{42,d} = [0\ \mathrm{m}, 4\ \mathrm{m}]^{\mathrm{T}}.$$

In Scenario 2, the desired relative-position offsets are

$$p_{10,d} = [-2\ \mathrm{m}, -4\ \mathrm{m}]^{\mathrm{T}}, \qquad p_{20,d} = [2\ \mathrm{m}, 4\ \mathrm{m}]^{\mathrm{T}},$$

$$p_{31,d} = [-2\ \mathrm{m}, -4\ \mathrm{m}]^{\mathrm{T}}, \qquad p_{42,d} = [2\ \mathrm{m}, 4\ \mathrm{m}]^{\mathrm{T}}.$$

In Scenario 3, the desired relative-position offsets are

$$p_{10,d} = [-3\ \mathrm{m}, -4\ \mathrm{m}]^{\mathrm{T}}, \qquad p_{20,d} = [3\ \mathrm{m}, 4\ \mathrm{m}]^{\mathrm{T}},$$

$$p_{31,d} = [-3\ \mathrm{m}, -4\ \mathrm{m}]^{\mathrm{T}}, \qquad p_{42,d} = [3\ \mathrm{m}, 4\ \mathrm{m}]^{\mathrm{T}}.$$

4.2. Comparison and Analysis

For each scenario, the proposed multi-point collision-avoidance method is compared with a conventional centroid-based single-point method. In Figures 7–12, panels (a) and (b) correspond to Scenario 1, panels (c) and (d) correspond to Scenario 2, and panels (e) and (f) correspond to Scenario 3. Panels (a), (c), and (e) show the results obtained with the proposed method, while panels (b), (d), and (f) show those obtained with the conventional method.

For a fair comparison, the two methods are evaluated under the same nominal vessel model, initial states, virtual-leader motion, external disturbances, obstacle configuration, observer and controller parameters, actuator constraints, and numerical settings. The principal difference between the two methods lies in the inter-vessel proximity measure used in the collision-avoidance APF. Specifically, the proposed method employs the minimum of the 16 pairwise distances generated by the bow, stern, port, and starboard characteristic points of two neighboring USVs, whereas the conventional method employs the centroid-to-centroid distance. Therefore, the comparison evaluates the effect of incorporating orientation-dependent characteristic-point information into the collision-avoidance mechanism.

To provide a consistent comparative assessment, the two methods are evaluated in terms of inter-vessel separation, formation-tracking error, control-input behavior, and collision occurrence. The corresponding inter-vessel distance responses, tracking errors, and control inputs are presented comparatively in Figures 8, 9 and 12, respectively, while the quantitative tracking-error indices and collision status are summarized in Table 2.

The proposed method constructs the inter-vessel repulsive potential terms using the point-based approximate proximity measure, i.e., the minimum of the 16 pairwise distances generated by the bow, stern, port, and starboard characteristic safety points of two neighboring USVs. The conventional method instead evaluates inter-vessel proximity using the centroid-to-centroid distance. Therefore, the comparison evaluates the benefit of incorporating additional orientation-dependent characteristic-point information into collision-risk assessment. The proposed measure is not interpreted as the exact hull-to-hull or ellipse-to-ellipse minimum distance.

Table 2. Quantitative comparison of formation tracking performance under the three simulation scenarios.

Scenario	Method	Error	Max. Error	Mean Error	Steady-State Error	Collision
1	Proposed method	e_{10}	3.59	1.04	0.93	No
		e_{20}	2.53	0.78	0.69	No
		e_{31}	3.34	1.01	0.90	No
		e_{42}	2.13	0.82	0.77	No
	Comparative method	e_{10}	2.02	N/A	N/A	Yes
		e_{20}	2.97	N/A	N/A	Yes
		e_{31}	2.05	1.86	1.96	Yes
		e_{42}	2.38	N/A	N/A	Yes
2	Proposed method	e_{10}	3.45	0.93	0.88	No
		e_{20}	1.82	0.35	0.27	No
		e_{31}	3.38	0.95	0.82	No
		e_{42}	3.24	0.40	0.16	No
	Comparative method	e_{10}	2.49	N/A	N/A	Yes
		e_{20}	3.74	N/A	N/A	Yes
		e_{31}	2.71	2.04	2.09	Yes
		e_{42}	2.93	N/A	N/A	Yes
3	Proposed method	e_{10}	4.03	1.14	1.18	No
		e_{20}	1.42	0.58	0.62	No
		e_{31}	3.90	1.23	1.16	No
		e_{42}	3.14	0.67	0.46	No
	Comparative method	e_{10}	3.01	N/A	N/A	Yes
		e_{20}	4.03	N/A	N/A	Yes
		e_{31}	3.31	2.30	2.37	Yes
		e_{42}	3.41	N/A	N/A	Yes

Note: N/A indicates that the corresponding mean and steady-state tracking errors cannot be meaningfully evaluated because collision occurrence causes the associated tracking errors to diverge. Here, e_{10}, e_{20}, e_{31}, and e_{42} denote the formation-tracking errors associated with the desired relative-position relationships between USV 1–USV 0, USV 2–USV 0, USV 3–USV 1, and USV 4–USV 2, respectively.

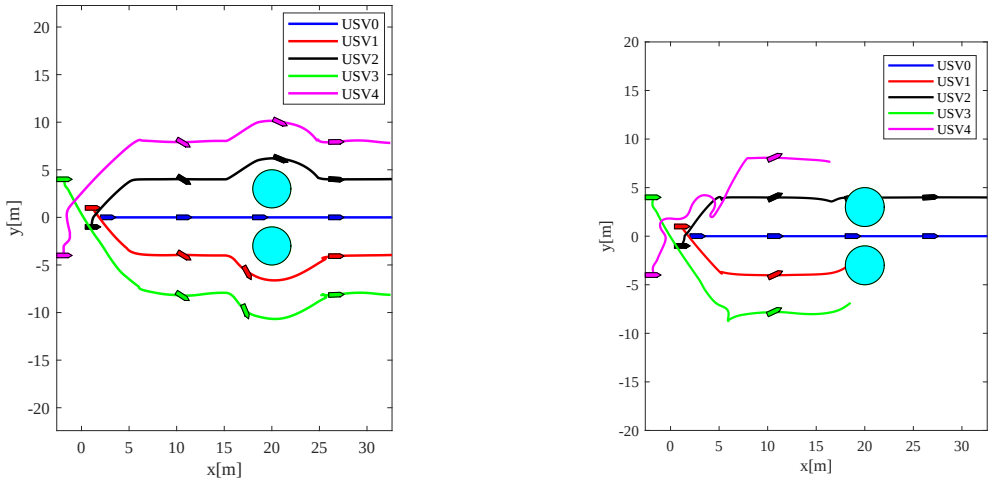


Figure 7. *Cont.*

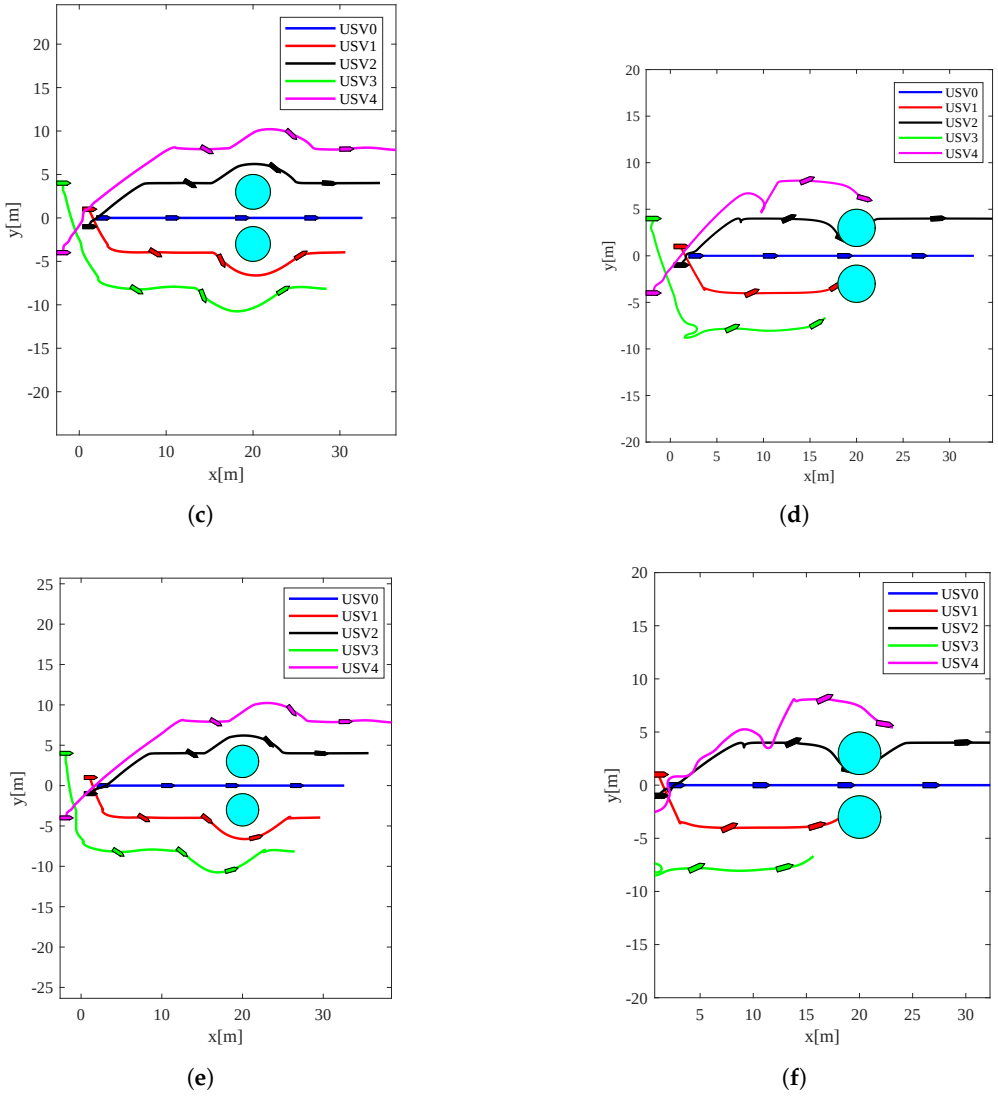


Figure 7. Formation trajectories with collision avoidance. (**a**) Formation control with Proposed method, Scenario 1. (**b**) Formation control with a conventional single-point collision avoidance method, Scenario 1. (**c**) Formation control with Proposed method, Scenario 2. (**d**) Formation control with a conventional single-point collision avoidance method, Scenario 2. (**e**) Formation control with Proposed method, Scenario 3. (**f**) Formation control with a conventional single-point collision avoidance method, Scenario 3.

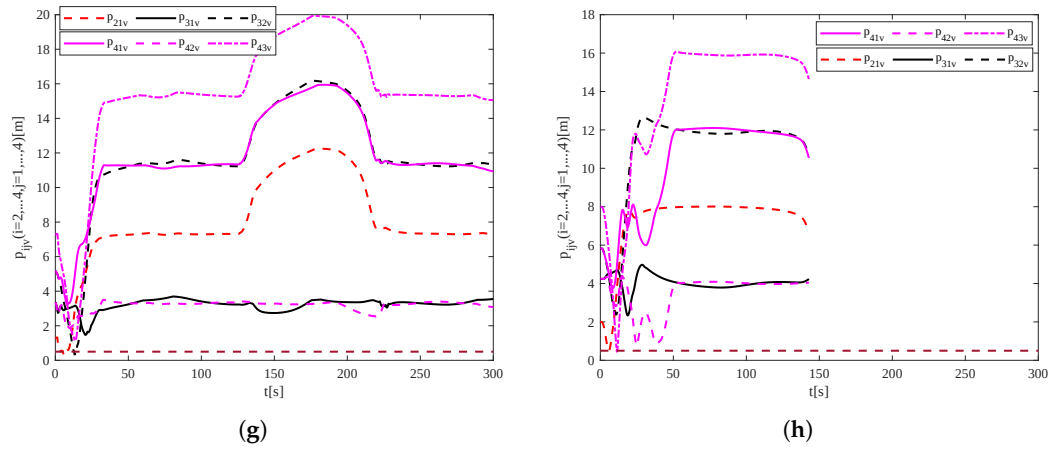


Figure 8. *Cont.*

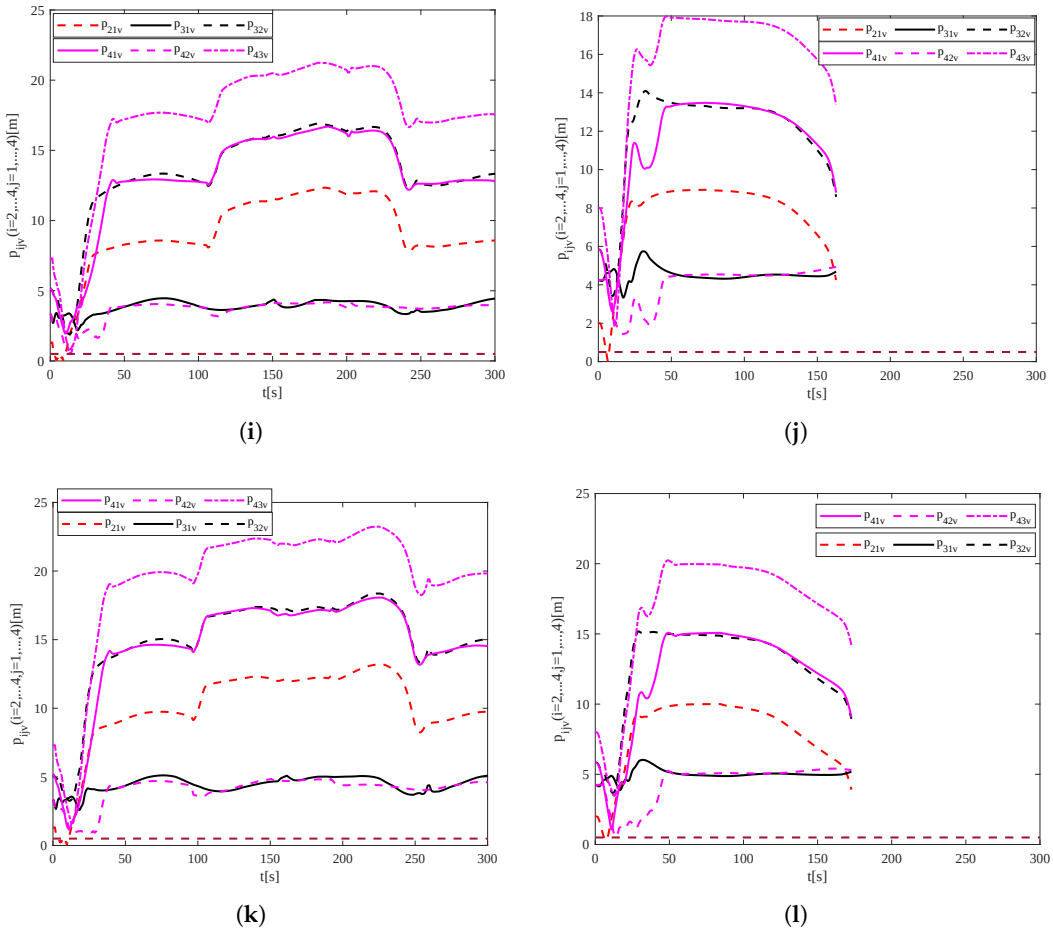


Figure 8. Inter-vessel proximity responses. (**a**) Formation control with Proposed method, Scenario 1. (**b**) Formation control with a conventional single-point collision avoidance method, Scenario 1. (**c**) Formation control with Proposed method, Scenario 2. (**d**) Formation control with a conventional single-point collision avoidance method, Scenario 2. (**e**) Formation control with Proposed method, Scenario 3. (**f**) Formation control with a conventional single-point collision avoidance method, Scenario 3.

To further complement the comparative evaluation with quantitative performance indices, the maximum, mean, and steady-state values of the formation tracking errors e_{10}, e_{20}, e_{31}, and e_{42} are summarized for the three simulation scenarios. In addition to the tracking-error indices, the collision status is also reported because collision avoidance constitutes a primary performance requirement of the considered formation control problem. The quantitative results are presented in Table 2.

As shown in Table 2, the proposed method maintains collision-free formation motion in all three scenarios, and all four formation tracking errors remain bounded throughout the simulations. In contrast, collisions occur when the comparative method is employed. After the collision, the tracking errors e_{10}, e_{20}, and e_{42} diverge, and therefore their mean and steady-state values cannot be meaningfully evaluated and are denoted by N/A in Table 2.

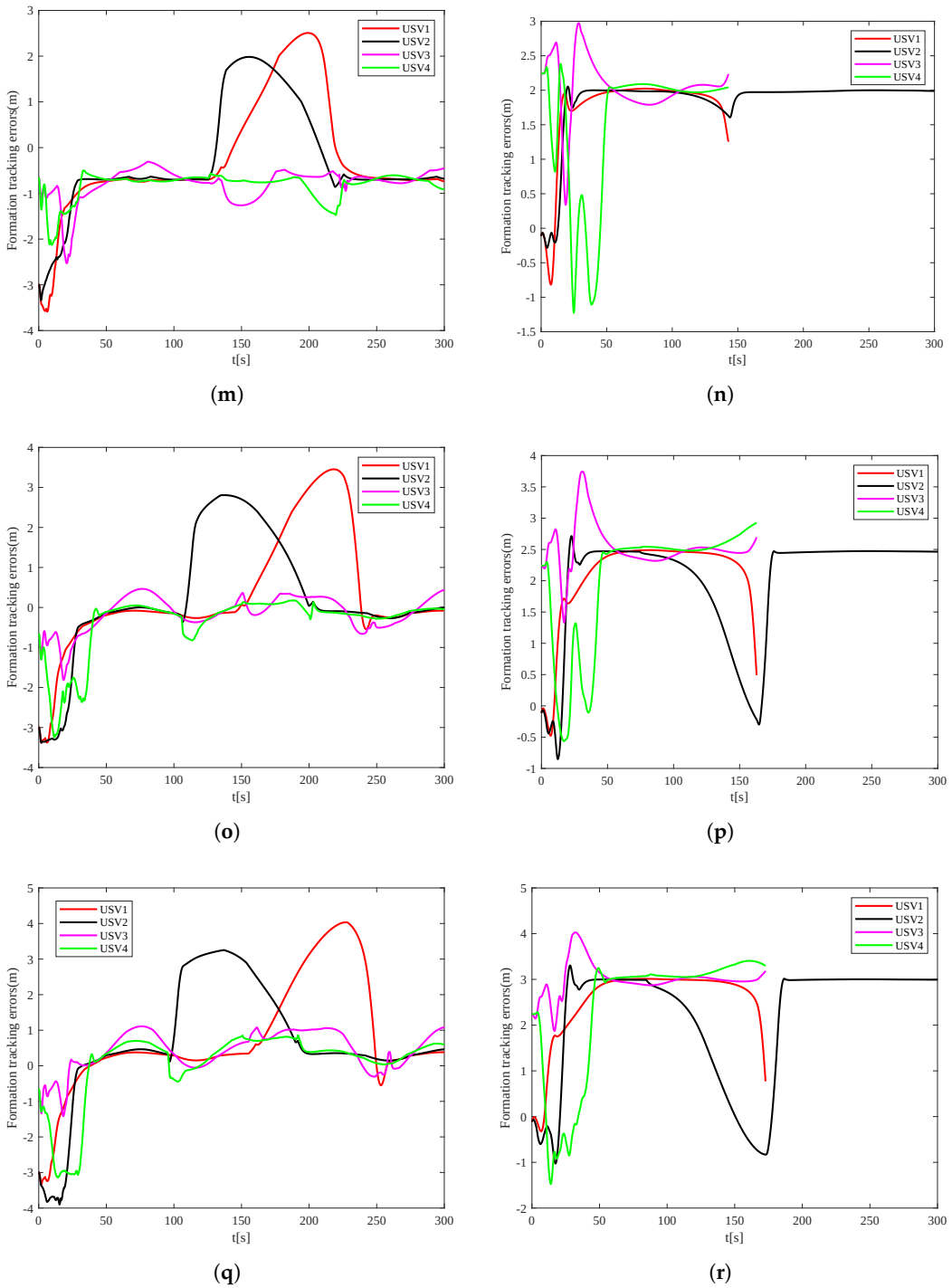


Figure 9. Formation tracking errors. (**a**) Formation control with Proposed method, Scenario 1. (**b**) Formation control with a conventional single-point collision avoidance method, Scenario 1. (**c**) Formation control with Proposed method, Scenario 2. (**d**) Formation control with a conventional single-point collision avoidance method, Scenario 2. (**e**) Formation control with Proposed method, Scenario 3. (**f**) Formation control with a conventional single-point collision avoidance method, Scenario 3.

For the tracking error e_{31}, for which the mean and steady-state values remain available for both methods, the proposed method yields mean errors of 1.01, 0.95, and 1.23 in Scenarios 1–3, respectively, compared with 1.86, 2.04, and 2.30 for the comparative method. Similarly, the corresponding steady-state errors obtained with the proposed method are 0.90, 0.82, and 1.16, whereas those of the comparative method are 1.96, 2.09, and 2.37.

Although the comparative method exhibits smaller maximum values of e_{31} in the three scenarios, these transient values do not imply successful formation operation because collisions subsequently occur. The results therefore demonstrate that the proposed method achieves a more favorable balance between collision avoidance and formation tracking, allowing temporary formation deviations when necessary while preserving collision-free and bounded formation motion.

Figure 7 presents the formation trajectories under the three desired formation geometries. As shown in panels (a), (c) and (e), the proposed method enables the follower USVs to complete the prescribed maneuvers while passing the two static obstacles and maintaining inter-vessel separation. During close-range encounters, the formations temporarily deform because the repulsive potential terms modify the nominal formation references. After the obstacle region has been passed, the followers gradually recover the desired relative configurations.

In contrast, the conventional-method trajectories in panels (b), (d) and (f) do not complete the prescribed maneuvers in the presented simulations. This behavior is consistent with the limitation of using only a centroid-based distance to represent close-range geometric separation. Ship-domain studies have emphasized the importance of direction-dependent navigational safety margins associated with different regions around a vessel [22,41]. In the present comparison, the centroid-to-centroid distance does not explicitly encode vessel-heading information or distinguish the local clearances associated with the bow, stern, port, and starboard regions. Therefore, the centroid distance may remain relatively large even when a pair of representative vessel extremities is already close during turning or crossing maneuvers. The corresponding repulsive action may consequently be activated later than that generated from the minimum safety-point distance. By evaluating all 16 safety-point pairs, the proposed measure responds to the closest pair among the selected bow, stern, port, and starboard characteristic points, rather than relying only on the distance between the two vessel centers.

Figure 8 presents the inter-vessel proximity responses. Panels (a), (c), and (e) show the minimum characteristic-point pairwise distances employed by the proposed method, whereas panels (b), (d), and (f) show the centroid-to-centroid distances used by the conventional method. During approximately the first 40 s, the vessels undergo an initial formation-adjustment transient. During this interval, the collision-avoidance terms temporarily have a higher priority than the formation-tracking objective, leading to evident variations in some distance responses. The collision-avoidance action is governed by the inter-vessel proximity measure defined in Section 2.5 together with the activation condition of the repulsive APF in Equation (9). When the corresponding proximity measure enters the prescribed activation range, i.e., $p_{ijv} \leq \bar{R}_c$, the inter-vessel repulsive potential is activated; otherwise, the corresponding potential term remains inactive.

During approximately 120–230 s, the follower USVs pass through the obstacle region and perform evident avoidance maneuvers. The distance variations during this interval are consistent with the temporary formation deformation observed in Figure 7. Since the left and right panels of Figure 8 use different distance definitions, their numerical values should not be compared directly. In particular, a centroid-to-centroid distance does not directly quantify the local clearances associated with the bow, stern, port, and starboard regions. Therefore, satisfaction of a centroid-distance condition alone does not necessarily indicate that all representative local vessel clearances are sufficiently large.

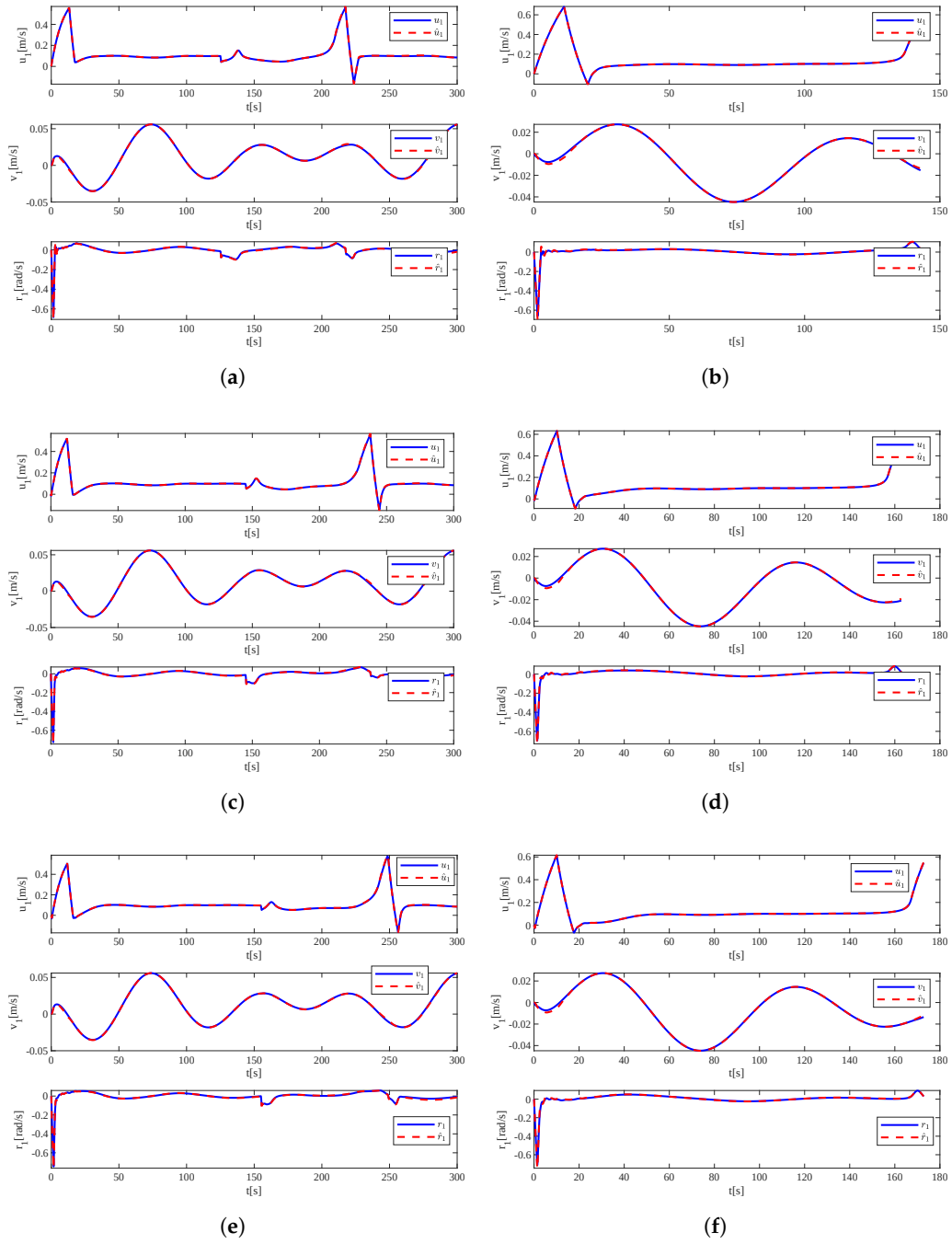


Figure 10. Velocity recovery performance of USV 1.(**a**) Formation control with Proposed method, Scenario 1. (**b**) Formation control with a conventional single-point collision avoidance method, Scenario 1. (**c**) Formation control with Proposed method, Scenario 2. (**d**) Formation control with a conventional single-point collision avoidance method, Scenario 2. (**e**) Formation control with Proposed method, Scenario 3. (**f**) Formation control with a conventional single-point collision avoidance method, Scenario 3.

The corresponding formation-tracking errors are shown in Figure 9. For the proposed method, the errors decrease after the initial formation adjustment and temporarily increase during the close-range avoidance interval. This increase occurs because collision and obstacle avoidance are assigned priority over formation tracking while the vessels pass the obstacle region. During approximately 230–300 s, the avoidance effects gradually decrease, and the formation-tracking errors approach small neighborhoods of zero.

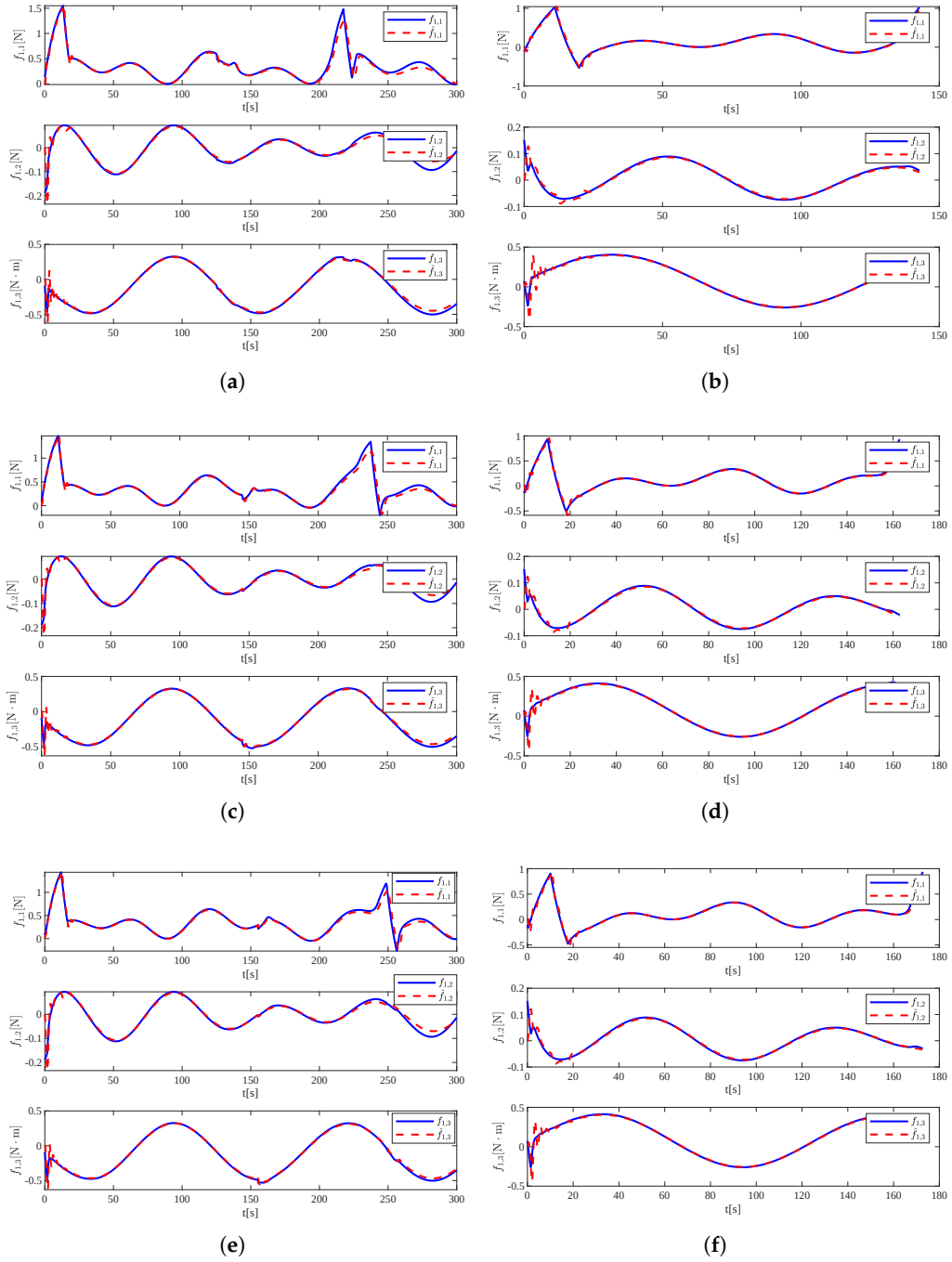


Figure 11. Unknown dynamics estimation performance of USV 1. (**a**) Formation control with Proposed method, Scenario 1. (**b**) Formation control with a conventional single-point collision avoidance method, Scenario 1. (**c**) Formation control with Proposed method, Scenario 2. (**d**) Formation control with a conventional single-point collision avoidance method, Scenario 2. (**e**) Formation control with Proposed method, Scenario 3. (**f**) Formation control with a conventional single-point collision avoidance method, Scenario 3.

For the conventional method, several response curves terminate before the prescribed simulation interval is completed, while the remaining formation-tracking errors do not approach zero. The combined results in Figures 7–9 indicate that the proposed method can complete the avoidance maneuvers and subsequently recover the desired formation under all three relative-position configurations.

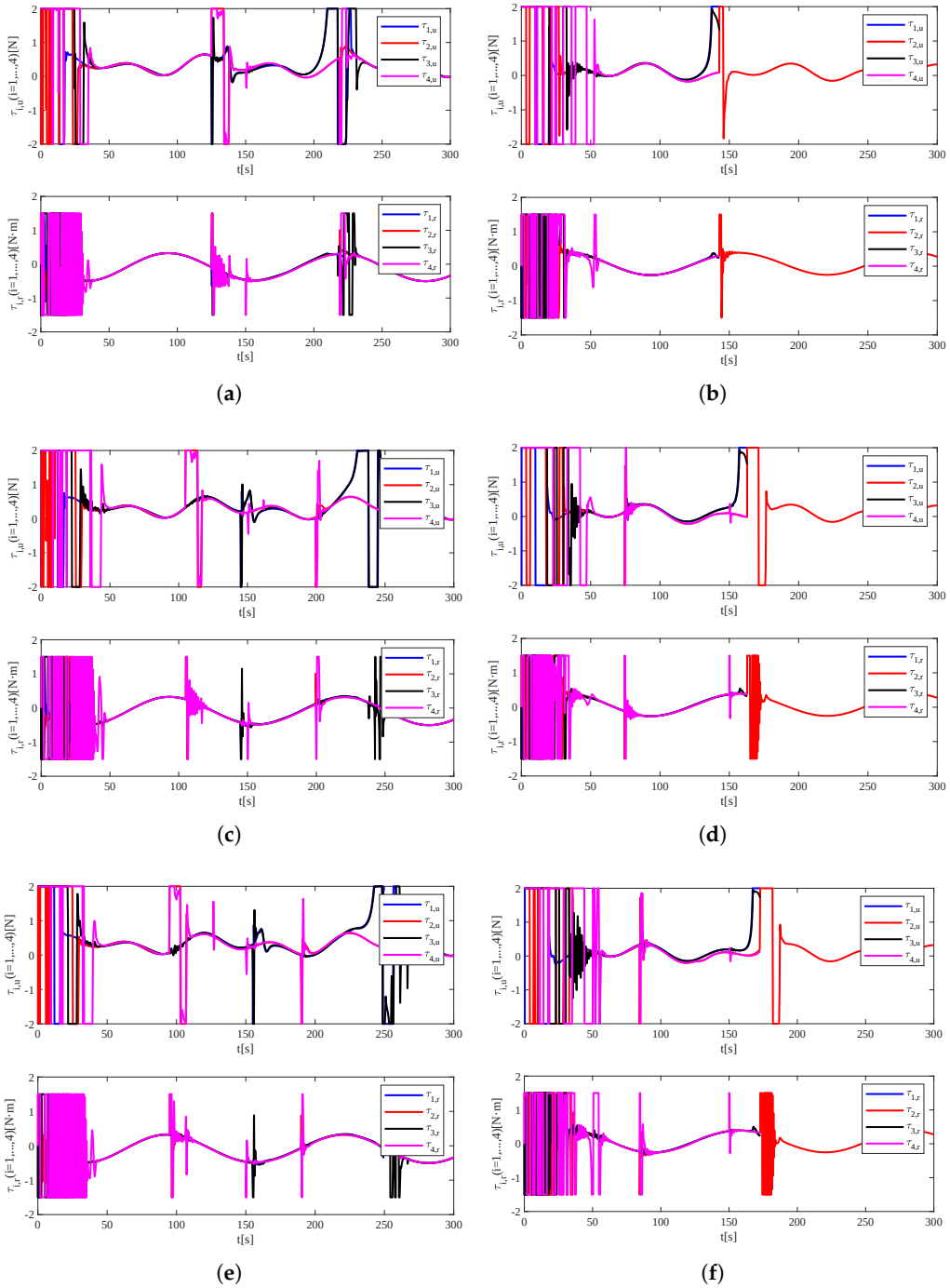


Figure 12. Control inputs. (**a**) Formation control with Proposed method, Scenario 1. (**b**) Formation control with a conventional single-point collision avoidance method, Scenario 1. (**c**) Formation control with Proposed method, Scenario 2. (**d**) Formation control with a conventional single-point collision avoidance method, Scenario 2. (**e**) Formation control with Proposed method, Scenario 3. (**f**) Formation control with a conventional single-point collision avoidance method, Scenario 3.

Figure 10 presents the velocity-estimation performance for USV 1. The estimated surge, sway, and yaw velocities closely follow their corresponding actual signals over the available simulation intervals. Small transient deviations appear during the initial formation adjustment and the obstacle-avoidance maneuvers, but the estimated signals remain bounded and rapidly approach the actual velocity responses. These results support the effectiveness of the proposed observer in recovering the unavailable velocity states from position–heading measurements.

Figure 11 presents the unknown dynamics estimation performance for USV 1. The estimated signals closely follow the corresponding actual lumped unknown dynamics signals, including during the initial transient and the close-range avoidance maneuvers. This indicates that the RBFNN-based observer can approximate the lumped effects of model uncertainties and external disturbances within the considered simulations.

Figure 12 presents the surge forces and yaw moments of the follower USVs. Relatively large control-input variations and temporary saturation occur mainly during the initial formation adjustment and the close-range avoidance maneuvers, when greater control effort is required to modify the vessel trajectories. Nevertheless, the applied surge forces and yaw moments remain within the prescribed actuator limits. The corresponding panels also provide a direct comparison of the control-input behavior of the proposed and conventional methods under the same actuator constraints.

Overall, the simulation results show that the proposed controller can complete the formation maneuvers in all three scenarios while simultaneously accounting for formation tracking, static-obstacle avoidance, inter-vessel separation, unavailable velocities, unknown dynamics, and actuator saturation. Compared with a centroid-only representation, the proposed multi-point measure provides additional information about orientation-dependent local vessel clearances during close-range formation maneuvers.

5. Conclusions

This paper has investigated the formation tracking control problem for underactuated USVs subject to unknown dynamics, external disturbances, inter-vessel collision risks, and input saturation. To improve the orientation-dependent geometric information available during close-range formation maneuvers, an elliptical disk-based collision-avoidance strategy has been developed by introducing a virtual elliptical reference geometry and four characteristic safety points corresponding to the bow, stern, port, and starboard directions of each vessel. Based on these characteristic points, APFs were constructed using the minimum of the corresponding point-pair distances as an approximate proximity measure, rather than relying only on centroid-to-centroid distances.

An observer-based distributed output feedback control scheme has been proposed by integrating a neural network-based observer, APFs, backstepping design, and auxiliary compensation terms. The observer was employed to recover unavailable velocity information and estimate lumped unknown dynamics using position–heading measurements only. Meanwhile, the auxiliary compensation terms were introduced to handle input saturation and underactuated dynamics without compromising the collision avoidance capability. The boundedness of all closed-loop error signals was rigorously established through Lyapunov analysis.

Comparative simulation results have demonstrated that the proposed controller can achieve formation tracking, obstacle avoidance, inter-vessel collision avoidance, and input saturation handling simultaneously. More importantly, compared with the conventional single-point collision-avoidance method, the proposed elliptical disk-based strategy maintains the prescribed characteristic point-based proximity threshold during the simulated close-range maneuvers, while no collision is observed in the considered simulations under the adopted characteristic point-based collision-avoidance criterion. This indicates that incorporating the bow, stern, port, and starboard characteristic-point information enables the controller to respond to orientation-dependent close-range collision risks that may not be adequately reflected by a centroid-based distance measure. Future work will focus on extending the proposed framework to dynamic obstacles, COLREGs-compliant encounter scenarios, and experimental validation on real USV platforms.

Author Contributions: Conceptualization, X.X. and Y.G.; methodology, Y.G. and X.X.; software, Y.G.; validation, Y.G. and X.X.; formal analysis, Y.G. and X.X.; investigation, Y.G.; writing—original draft preparation, Y.G.; writing—review and editing, X.X. and Y.G.; visualization, Y.G.; supervision, X.X.; project administration, X.X. All authors have read and agreed to the published version of the manuscript.

Funding: This research received no external funding.

Data Availability Statement: The data presented in this study are available on request from the corresponding author.

Conflicts of Interest: The authors declare no conflicts of interest.

References

1. Liu, Z.; Zhang, Y.; Yu, X.; Yuan, C. Unmanned Surface Vehicles: An Overview of Developments and Challenges. *Annu. Rev. Control* **2016**, *41*, 71–93. [CrossRef]
2. Oh, K.K.; Park, M.C.; Ahn, H.S. A Survey of Multi-Agent Formation Control. *Automatica* **2015**, *53*, 424–440. [CrossRef]
3. Yan, X.; Jiang, D.; Miao, R.; Li, Y. Formation Control and Obstacle Avoidance Algorithm of a Multi-USV System Based on Virtual Structure and Artificial Potential Field. *J. Mar. Sci. Eng.* **2021**, *9*, 161. [CrossRef]
4. Cui, R.; Ge, S.S.; How, B.V.E.; Choo, Y.S. Leader–Follower Formation Control of Underactuated Autonomous Underwater Vehicles. *Ocean Eng.* **2010**, *37*, 1491–1502. [CrossRef]
5. Jin, X. Fault Tolerant Finite-Time Leader–Follower Formation Control for Autonomous Surface Vessels with LOS Range and Angle Constraints. *Automatica* **2016**, *68*, 228–236. [CrossRef]
6. Xia, G.; Sun, C.; Zhao, B.; Xia, X.; Sun, X. Neuroadaptive Distributed Output Feedback Tracking Control for Multiple Marine Surface Vessels with Input and Output Constraints. *IEEE Access* **2019**, *7*, 123076–123085. [CrossRef]
7. Dong, W. Cooperative Control of Underactuated Surface Vessels. *IET Control Theory Appl.* **2010**, *4*, 1569–1580. [CrossRef]
8. Park, B.S.; Yoo, S.J. An Error Transformation Approach for Connectivity-Preserving and Collision-Avoiding Formation Tracking of Networked Uncertain Underactuated Surface Vessels. *IEEE Trans. Cybern.* **2019**, *49*, 2955–2966. [CrossRef] [PubMed]
9. Xia, G.; Xia, X.; Zhao, B.; Sun, C.; Sun, X. Distributed Tracking Control for Connectivity-Preserving and Collision-Avoiding Formation Tracking of Underactuated Surface Vessels with Input Saturation. *Appl. Sci.* **2020**, *10*, 3372. [CrossRef]
10. Dai, Y.; Kim, Y.; Wee, S.; Lee, D.; Lee, S. A Switching Formation Strategy for Obstacle Avoidance of a Multi-Robot System Based on Robot Priority Model. *ISA Trans.* **2015**, *56*, 123–134. [CrossRef] [PubMed]
11. Tran, V.P.; Garratt, M.A.; Petersen, I.R. Switching Formation Strategy with the Directed Dynamic Topology for Collision Avoidance of a Multi-Robot System in Uncertain Environments. *IET Control Theory Appl.* **2020**, *14*, 2948–2959. [CrossRef]
12. Dai, S.L.; He, S.; Lin, H.; Wang, C. Platoon Formation Control with Prescribed Performance Guarantees for USVs. *IEEE Trans. Ind. Electron.* **2018**, *65*, 4237–4246. [CrossRef]
13. He, S.; Wang, M.; Dai, S.L.; Luo, F. Leader–Follower Formation Control of USVs with Prescribed Performance and Collision Avoidance. *IEEE Trans. Ind. Inform.* **2019**, *15*, 572–581. [CrossRef]
14. Liang, X.; Qu, X.; Wang, N.; Li, Y.; Zhang, R. Swarm Control with Collision Avoidance for Multiple Underactuated Surface Vehicles. *Ocean Eng.* **2019**, *191*, 106516. [CrossRef]
15. Peng, Z.; Wang, D.; Li, T.; Han, M. characteristic point-based Cooperative Formation Maneuvering of Autonomous Surface Vehicles with Connectivity Preservation and Collision Avoidance. *IEEE Trans. Cybern.* **2020**, *50*, 2527–2535. [CrossRef] [PubMed]
16. Jo, H.J.; Kim, S.R.; Kim, J.H.; Park, J.Y. Comparison of Velocity Obstacle and Artificial Potential Field Methods for Collision Avoidance in Swarm Operation of Unmanned Surface Vehicles. *J. Mar. Sci. Eng.* **2022**, *10*, 2036. [CrossRef]
17. Tang, X.; Yu, J.; Li, X.; Dong, X.; Ren, Z. Distributed Formation Control with Obstacle Avoidance for Multiple Underactuated Unmanned Surface Vehicles. *J. Frankl. Inst.* **2024**, *361*, 107008. [CrossRef]
18. Tee, K.P.; Ge, S.S.; Tay, E.H. Barrier Lyapunov Functions for the Control of Output-Constrained Nonlinear Systems. *Automatica* **2009**, *45*, 918–927. [CrossRef]
19. Do, K.D. Formation Control of Multiple Elliptical Agents with Limited Sensing Ranges. *Automatica* **2012**, *48*, 1330–1338. [CrossRef]
20. Do, K.D. Formation Control of Underactuated Ships with Elliptical Shape Approximation and Limited Communication Ranges. *Automatica* **2012**, *48*, 1380–1388. [CrossRef]
21. Wang, N. An Intelligent Spatial Collision Risk Based on the Quaternion Ship Domain. *J. Navig.* **2010**, *63*, 733–749. [CrossRef]
22. Deng, F.; Jin, L.; Hou, X.; Wang, L.; Li, B.; Yang, H. COLREGs: Compliant Dynamic Obstacle Avoidance of USVs Based on the Dynamic Navigation Ship Domain. *J. Mar. Sci. Eng.* **2021**, *9*, 837. [CrossRef]
23. Yoo, S.J.; Park, B.S. Distributed dynamic obstacle avoidance design to connectivity-preserving formation control of uncertain underactuated surface vehicles under a directed network. *Ocean Eng.* **2023**, *273*, 113872. [CrossRef]

24. Liu, S.; Zhang, G.; Guo, G.; Li, J. Adaptive output-feedback event-triggered formation control for underactuated ships with obstacle avoidance mechanism. *Ocean Eng.* **2024**, *299*, 117373. [CrossRef]
25. Xue, J.; Song, Y.; Hu, H. Formation Control of a Multi-Unmanned Surface Vessel System: A Bibliometric Analysis. *J. Mar. Sci. Eng.* **2024**, *12*, 1484. [CrossRef]
26. Park, B.S.; Kwon, J.W.; Kim, H. Neural Network-Based Output Feedback Control for Reference Tracking of Underactuated Surface Vessels. *Automatica* **2017**, *77*, 353–359. [CrossRef]
27. Xia, G.; Xia, X.; Sun, X. Formation Control with Collision Avoidance for Underactuated Surface Vehicles. *Asian J. Control* **2022**, *24*, 2244–2257. [CrossRef]
28. Seshagiri, S.; Khalil, H.K. Output Feedback Control of Nonlinear Systems Using RBF Neural Networks. *IEEE Trans. Neural Netw.* **2000**, *11*, 69–79. [CrossRef] [PubMed]
29. Fossen, T.I. *Handbook of Marine Craft Hydrodynamics and Motion Control*, 2nd ed.; John Wiley & Sons: Chichester, UK, 2021. [CrossRef]
30. Zheng, Z.; Huang, Y.; Xie, L.; Zhu, B. Adaptive Trajectory Tracking Control of a Fully Actuated Surface Vessel with Asymmetrically Constrained Input and Output. *IEEE Trans. Control Syst. Technol.* **2018**, *26*, 1851–1859. [CrossRef]
31. Fu, M.; Yu, L. Finite-time extended state observer-based distributed formation control for marine surface vehicles with input saturation and disturbances. *Ocean Eng.* **2018**, *159*, 219–227. [CrossRef]
32. Kowalczyk, W.; Michałek, M.; Kozłowski, K. Trajectory Tracking Control and Obstacle Avoidance for a Differentially Driven Mobile Robot. *IFAC Proc. Vol.* **2011**, *44*, 1058–1063. [CrossRef]
33. Ghommam, J.; Saad, M.; Mnif, F. Prescribed performances based fuzzy-adaptive output feedback containment control for multiple underactuated surface vessels. *Ocean Eng.* **2022**, *249*, 110898. [CrossRef]
34. Wu, G.X.; Ding, Y.; Tahsin, T.; Atilla, I. Adaptive neural network and extended state observer-based non-singular terminal sliding modetracking control for an underactuated USV with unknown uncertainties. *Appl. Ocean. Res.* **2023**, *135*, 103560. [CrossRef]
35. Peng, Z.; Wang, J.; Wang, D. Distributed Containment Maneuvering of Multiple Marine Vessels via Neurodynamics-Based Output Feedback. *IEEE Trans. Ind. Electron.* **2017**, *64*, 3831–3839. [CrossRef]
36. Krstic, M.; Kanellakopoulos, I.; Kokotovic, P.V. *Nonlinear and Adaptive Control Design*; John Wiley & Sons: New York, NY, USA, 1995.
37. Wang, N.; Ki Ahn, C. Hyperbolic-Tangent LOS Guidance-Based Finite-Time Path Following of Underactuated Marine Vehicles. *IEEE Trans. Ind. Electron.* **2020**, *67*, 8566–8575. [CrossRef]
38. Fossen, T.I.; Breivik, M.; Skjetne, R. Line-of-Sight Path Following of Underactuated Marine Craft. *IFAC Proc. Vol.* **2003**, *36*, 211–216. [CrossRef]
39. Swaroop, D.; Hedrick, J.K.; Yip, P.P.; Gerdes, J.C. Dynamic Surface Control for a Class of Nonlinear Systems. *IEEE Trans. Autom. Control* **2000**, *45*, 1893–1899. [CrossRef]
40. Skjetne, R.; Fossen, T.I.; Kokotović, P.V. Adaptive maneuvering, with experiments, for a model ship in a marine control laboratory. *Automatica* **2005**, *41*, 289–298. [CrossRef]
41. Wang, Z.; Huang, W.; Im, N. Physics-Driven Collision Risk Evaluation of Autonomous Surface Vehicles Using Quaternion Ship Domain and Geometric-Temporal Indicators. *J. Mar. Sci. Eng.* **2025**, *13*, 2146. [CrossRef]

Disclaimer/Publisher's Note: The statements, opinions and data contained in all publications are solely those of the individual author(s) and contributor(s) and not of MDPI and/or the editor(s). MDPI and/or the editor(s) disclaim responsibility for any injury to people or property resulting from any ideas, methods, instructions or products referred to in the content.